UAV-based Post-disaster Damage Assessment of Buildings Using Image Processing

by

Seyed Danial Jozi

A thesis submitted in partial fulfillment of the requirements for the degree of

Master of Science

in

Structural Engineering

Department of Civil and Environmental Engineering
University of Alberta

Abstract

The extensive damages caused by natural disasters incur substantial costs to the built environment. The escalating frequency and severity of disasters, particularly hurricanes, driven by the impacts of Climate Change, highlight the urgency for prompt post-disaster assessments. A thorough and rapid post-disaster assessment plays a crucial role in facilitating the swift evaluation of the situation, and enables the determination of the extent of damage for each component in the built environment. To address this need, this study proposes an image-processing-based method utilizing Unmanned Aerial Vehicle (UAV) imagery of solely the post-disaster situation for the automated evaluation of the building damage. The suggested approach accordingly utilizes single post-disaster imagery of the buildings, and integrates texture-based features, encompassing texture dissimilarity and homogeneity, along with edge-based features. Canny edge detection is employed to introduce novel indices that gauge irregularity by assessing entropy of the detected edges and uniformity in the distribution of edge line orientations. These features are then input into a Naïve Bayesian Classification process, allowing for the classification of damaged and undamaged classes while accommodating the underlying uncertainties. The proposed method exhibits a validation accuracy of 91.3 percent when applied to unidentified building images, effectively distinguishing between damaged and undamaged structures. In addition, the functionality of the proposed method has been evaluated through application on a real-life post-disaster scene. The results underscore the potential efficacy of utilizing UAV-captured images and advanced image processing techniques for rapid and accurate post-disaster damage assessment.

Preface

A part of this research has been presented at the CSCE Annual Conference 2023 in Moncton, New Brunswick, and a conference paper titled "UAV-based Post-disaster Damage Assessment of Residential Buildings using Image Processing" has been written under the authorship of Dr. Nima Shirzad-Ghaleroudkhani and co-authorship of Dr. Shaghayegh Abtahi, Dr. Mustafa Gül and Garvit Luhadia.

A paper incorporating this whole thesis titled "UAV-based Post-disaster Damage Assessment of Residential Buildings using Image Processing" has been submitted to the International Journal of Disaster Risk Reduction, currently being under review. The paper has been written under the co-authorship of Dr. Nima Shirzad-Ghaleroudkhani, Dr. Shaghayegh Abtahi, Dr. Mustafa Gül and Garvit Luhadia.

Acknowledgements

Table of Contents

List of Tables

List of Figures

viii

Chapter 1. Introduction

Disasters happen all around the world from time to time. Causing multiple damages, leaving people without supplies and even resulting in casualties, disasters can neither be resisted nor eradicated. However, by having the necessary tools, the aftermaths can be controlled and the consequent financial losses can be minimized. As a result, this research plans to take one step further in the post-disaster damage assessment process. In this section, the importance of rapid post-disaster assessment has been outlined by focusing on the increasing severity of disasters and their unfortunate outcomes.

1.1 Background and Motivation

Climate change, having had global impacts since the last century, is increasingly causing inevitable substantial costs in the modern world. Within the context of natural disasters, the rising global temperatures result in a higher temperature of ocean waters and consequently, rise in the ocean levels and moisture in the air. While the risen ocean levels result in more floods, the risen ocean temperatures and moisture level amplify the intensity of hurricanes, making them more destructive and unpredictable. According to NASA [1], the additional vapor in the air fuels the hurricane by creating more intense rainfalls. It is also mentioned that even though the frequency of hurricanes have remained rather unchanged, the intensity and category number of the hurricanes are increasing. In another example, researchers have found that compared to 100 years ago, the frequency of destructive hurricanes has tripled in the United States [2]. In Canada, it has been estimated by the Insurance Bureau of Canada (IBC) that 8 of the 10 costliest weather events in the country have all happened in the past 10 years (since 2013) when considering the insured financial loss resulted from the damages [3][4], as illustrated in Table 1-1.

Table 1-1. The 10 Costliest Natural Disasters in Canada

	Disaster	Year	Insured Loss (CAD)
1	Fort McMurray Wildfires	2016	4 billion
2	Eastern Ice Storm	1998	2.3 billion
3	Southern Alberta Floods	2013	1.8 billion
4	Alberta Hailstorm	2020	1.2 billion
5	Toronto Flood	2013	1 billion
6	Ontario-Quebec Windstorm	2022	1 billion
7	Hurricane Fiona	2022	800 million
8	Toronto Flood	2005	780 million
9	Ontario Windstorm	2018	695 million
10	BC Flood	2021	675 million

The Insurance Bureau of Canada has ranked 2022 as the third worst year of Canadian history in terms of insured damages, only behind the years 2016 and 2013, with a massive cost of 3.1 billion Canadian dollars. The organization outlines that the severe weather has been hugely responsible for this loss [5], as it could be seen that the most expensive disasters in this year have been the Windstorm of Ontario-Quebec and Hurricane Fiona, both being weather-related events. In addition, the organization has estimated that the overall trend in insured catastrophic losses in Canada has been increasing since 1990, and is predicted to grow in the following years [5]. Many

studies have investigated the correlation between climate change and the economic costs of hurricanes [6]. For illustration, Hurricane Fiona's 2022 strike on the Caribbean and Atlantic Canada resulted in over 25 casualties, displaced 13000 individuals, and costed approximately 4 billion Canadian dollars in damages. This has been the costliest disaster to ever happen in the region of Atlantic Canada [7]. Furthermore, Knutson et al. [8] have predicted a surge in the intensity of hurricanes by the year 2100. As an instance, Hurricane Ian which took its toll on Cuba and southern United States in 2022, caused more than 130 casualties and became the fifth strongest hurricane to ever hit United States. This hurricane has been the most severe and expensive in Florida since 1992 and displaced more than 40,000 people. Hurricane Ian is an illustration of how climate change is impacting the severity and strength of hurricanes. Looking specifically at the Atlantic basin, the 24-hour intensification of the 5 percent strongest hurricanes is around 16 km/h stronger compared to 30 years ago [7]. Fig. 1-1 shows the destruction caused by Hurricane Maria in the island of Dominica in 2017.

Fig. 1-1. Destruction caused by Hurricane Maria in Roseau, Dominica in 2017 [9]

In addition to the weather-induced natural disasters, earthquakes result in tremendous financial losses and numerous casualties. In this regard, the earthquake and consequent tsunami

that struck the Tōhoku region of Japan in 2011, has been responsible for the direct damage cost of 211 billion US dollars and stands as the costliest natural disaster ever taking place [10]. As a consequence, there is a growing importance in the development and employment of rapid Post-Disaster Assessment to control the aftermath of such events, smoothen the search and rescue process and limit the casualties. Such disasters are also followed by smaller events, such as the aftershocks, which result in more casualties. In case the damage and safety of structures can be identified immediately after the main event, people can be prevented from entering structures with questionable status and more lives could be saved.

At the current state, the process of post-disaster assessment and damage recognition profoundly relies on visual inspection and post-disaster surveys, requiring a substantial amount of workforce from experts and skilled personnel [11]. In other words, the process is mostly done manually and with manpower. However, this approach to post-disaster assessment exhibits inefficiency both in terms of time consumption and resource utilization, while exposing the life of crew to danger [12][13]. Moreover, the most severely affected regions frequently encounter accessibility issues due to debris and obstructed roads, impeding a prompt entry and therefore, deterring a thorough evaluation of damages. As a result, a delay is expected in the post-disaster assessment process which has the potential of amplifying losses and casualties. This fact emphasizes the critical need for improvements in the overall efficiency of these assessments. [12]. As an illustrative example, nearly six days were required for the ground crews assigned to damage assessment of Hurricane Irma in Florida to cover only a portion of affected areas, which included the regions surrounding Gulf Coast, Atlantic Coast and Florida Keys [14]. Hence, there is an immediate need for a rapid, automated and uninterrupted post-disaster assessment to accurately

identify damaged areas in a brief amount of time, thus optimizing search and rescue operations and limiting the losses.

1.2 Objectives

This study attempts to create a framework for rapid post-disaster damage assessment of residential houses, which is based on the post-disaster imagery collected by Unmanned Aerial Vehicle (UAV) or commonly known as drone. The intension is to construct a method for analyzing the houses within drone imagery and identify their corresponding damage state. The study focuses on the building image analysis and classification, and for this purpose, aims to extract features and build identifying indices from the building images. For a rapid post-disaster assessment, a computationally-light method would be typically required and in this regard, the study employs solely image processing to define the indicative parameters for each image. Moreover, the study aims to utilize a quick and straightforward probability-based classifier, the result of which being a percentage showing the probability of each building being damaged.

In order to perform the assessment process as resource-efficient and time-efficient as possible, a sole single-view post-disaster drone image of each building is sufficient, meaning that neither the pre-disaster imagery of the buildings nor multiple views of a building are required to identify whether the building is damaged or not. Accordingly, a single image of each building undergo a set of image processing techniques, and 4 indicative indices are subsequently achieved, which are further used in a probability-based classifier to identify the damage state of each building. Utilization of image processing techniques requires fewer amount of data to be trained in comparison to models with deeper learning strategies. In addition, image processing techniques provide a platform which is light in terms of computation, can be adjusted or expanded

conveniently, and can produce reliable results considering that the outputted features directly contribute to understanding the damage state.

The method developed in this study specifically detects the damaged residential buildings after a disaster, most prominently hurricane. The outcomes derived from this method can subsequently serve as an initial step for the post-disaster inspection and enhanced decision-making, alongside other applications such as cost estimation and resilience. When combined with a proper tool for detecting and localizing the buildings, the method has the ability to aid in decision-making by providing the location of damaged houses and therefore, facilitate the disaster recovery process in a way that the struck houses can receive aid sooner. In addition, the method is able to provide an overall estimation of the costs considering the abundance of struck houses, as well as the overall cost of the disaster. A rebuilding plan could also be better adjusted according to the estimated damage. As a result, the utilization of this model could be beneficial for governmental and municipal organizations which need to properly plan for disaster recovery, as well as other particular organizations such as insurance companies which need an estimation of the costs.

In the following sections of the study, the current research carried out in terms of post-disaster assessment have been outlined, the utilized methodology for image processing and classification has been narrated, followed by the results and a real-life application where the method has proven to function successfully. At the end, the conclusion along with the limitations and possible future growths of the study have been mentioned. A rapid fully-automated post-disaster would not be out of reach with the proposed framework of this study.

Chapter 2. Literature Review

As mentioned in the previous section, a rapid post-disaster assessment method is vital to address the increasing severity of natural disasters and their consequent damages and casualties. There are two crucial steps to achieve this outcome, consisting of the data collection and data analysis. Together, these two steps insure the readiness of the data necessary to recognize the damage, and the recognition of damaged areas and places.

Historically, the post-disaster assessment has been mostly performed manually, meaning that it is remarkably based on manpower-sourced field surveys [11][12][13], which as mentioned in the previous section, comes short in both efficiency and safety. Moreover, the approach to perform the data collection and to identify damages by collecting ground-view images of the disaster-struck region is not quite feasible, since in the aftermath of a disaster, obtaining ground-view images could be challenging due to obstructed pathways and debris, meaning that the most severely-struck regions are usually the hardest ones to access. Therefore, the research has been more focused towards the utilization of *Remote Sensing* imagery, and in the recent decades, the employment of Remote Sensing technologies has been gaining more popularity in the event of natural disasters [15]. The damage detection includes direct or indirect approaches [15]. Indirect approaches are rather focused on the detection of whole or larger-scale damaged urban areas with substitute measures such as the night-time lighting level [15][16][17], while direct approaches are directly focused on the damage of buildings, as investigated in this study. Many approaches exist in order to collect the remote sensing images, including *Optical Satellite images*, *Synthetic Aperture Radar (SAR) images*, and *Unmanned Aerial Vehicle (UAV) images* [18][19]. These types of images comprise a broad, and meanwhile, detailed view of different regions, enabling the recognition of damage across various sections. In the meantime, collection of these images can be done

uninterruptedly in the aftermath of a disaster as opposed to the ground-view images, and incorporate significant lower risk [15][18]. Fig 2-1 illustrates a sample remote sensing image from a flooded region in Malaysia. Each of these remote sensing approaches, along with their strengths and weaknesses are described in this chapter.

Fig. 2-1: Sample remote sensing image from a flooded region in Malaysia (Source: Pexels, Pok Rie [20])

2.1 Remote Sensing Imagery

2.1.1 Optical Satellite Imagery

The utilization of optical satellite imagery for the post-disaster assessment has been frequently researched. A sample satellite imagery from an urban area in Mexico has been presented in Fig. 2-2. As a classic approach, *visual interpretation* of the satellite imagery can be used for damage detection is the structures [21]. However, this process could be challenging and time-consuming when dealing with higher levels of spatial resolution, limiting coverage over large areas [22].

Nonetheless, visual interpretation is against the desired rapid and uninterrupted post-disaster assessment process.

A more effective approach using satellite imagery is *change detection*, which necessitates the acquisition of both pre- and post-disaster images. In this method, various techniques (e.g. Machine Learning) are applied to post-classification images to distinguish alterations between the two scenarios [21]. Another approach involves *data mining* on images. This involves extracting particular features through image processing and utilizing them for conducting comparisons [23]. As an example of using change detection in satellite images, Sublime et al. [13] researched the possibility of detecting the areas destroyed by the Tsunami of Tohoku in 2011. This research which acquired the real-time satellite images before and after the event, proposed a deep-learning-based method in order to identify the affected areas by the automatic recognition of changes within the images. In a research done by Lee et al. [24], a semi-supervised learning approach fueled by the pre- and post-disaster images is used to detect the damage. The paper investigates disasters such as earthquake, armed conflict and wildfire. Another study done by Oludare et al. [25] proposed a semi-supervised model for factoring in the various housing styles and unseen images. By capturing information from a large amount of unlabeled data and satellite images, their proposed model has outperformed the ability of a base model which consists of a two-stream high-resolution network and intakes both the pre- and post-disaster images.

In a rather different approach, Shao et al. [26] developed a deep convolutional neural network model which performs a remote sensing pixel-classification based on satellite imagery. The system has been created in a way to autonomously categorize each pixel inside a post-disaster image into one of three classes of undamaged building, damaged building, or background. For this study, the network takes both pre- and post-disaster images as input to enhance semantic information, and

optimization of the network involves employing a hybrid loss function, enabling the system to recognize damaged buildings. A more recent study done by Shen et al. [27] also incorporated convolutional neural networks but with a different approach, and by factoring in the correlation between the pre- and post-disaster images. The method first extracts the buildings and their locations from satellite images, and then a cross-directional attention module is built to explore the correlation between pre- and post-disaster images which are fed to the system separately. This correlation results in the damage class identification of disasters such as flood and hurricane. Cao et al. [28] proposed a convolutional neural network model for assessing the flooded houses in the aftermath of hurricane. The study comprises square-sized images of buildings, which are either flooded/damaged or undamaged, and uses the database to train and validate the model.

While the majority of mentioned studies have had a deeper focus on buildings themselves, Ghaffarian et al. [29] investigated the identification of debris for the damage and recovery assessment. Their study involved very high resolution satellite images to identify the debris, their type and time of removal, through a number of various textural analysis procedures. The study concluded that the Histogram of Oriented Gradients, which found the gradients on the image for each point on the image, had the highest accuracy in detecting the debris. In another study, Dotel et al. [30] investigated the change in topographic features such as roads to identify the damaged regions, focusing mainly on water-induced disasters such as hurricanes and floods. The outcome is achieved by incorporating convolutional neural networks to perform semantical segmentation on the topographic regions. Berezina et al. [31] utilized very high resolution satellite images in their study and with the use of coupled convolutional neural networks, they generated the pre-hurricane building footprints and performed a deep-learning-based classification to identify the damaged buildings.
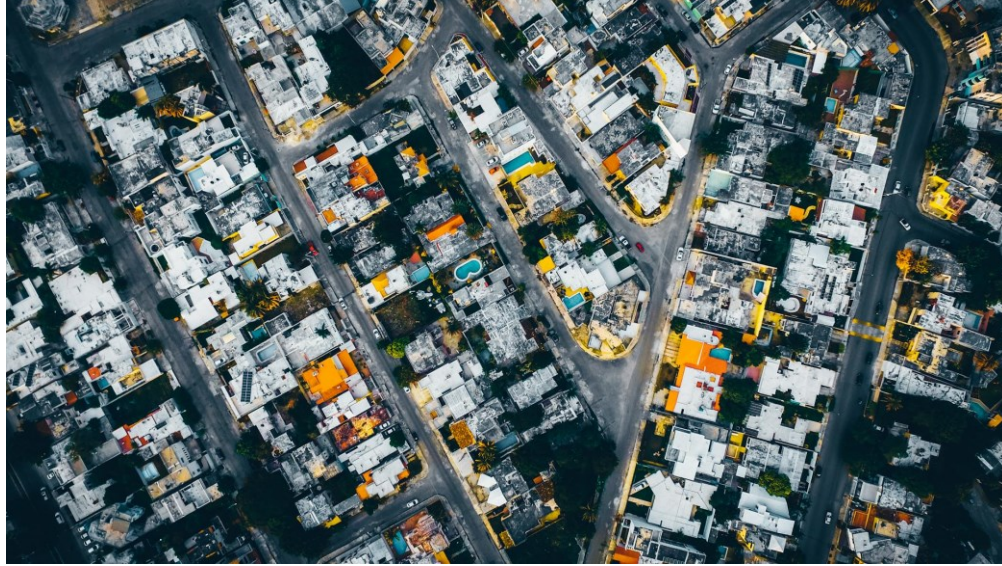
Fig. 2-2: Sample optical satellite image from an urban area in Mexico (Source: Pexels, Jorge Zapata [32]**)**

While the aforementioned studies have mainly focused on post-disaster assessment based on both the pre- and post-disaster images, the post-disaster assessment that utilizes satellite imagery can also be accomplished using solely post-disaster images. This has been demonstrated by Zhang et al. [33] in the detection of damaged buildings following an earthquake. In their study, which is based on the difference of textural heterogeneity in original buildings and damaged regions, satellite images are enhanced to reach a desired feature level and then a damage index is introduced to detect damaged buildings by the fusion of those features. The features utilized are mainly based on the texture of the images. The study reaches an accuracy of 76.75 percent for detecting the post-earthquake damaged buildings. Another instance of the sole use of post-disaster images is a novel study done by Tilon et al. [34], an unsupervised machine learning model has been utilized to differentiate the damaged and undamaged buildings after various types of disasters. The study uses a mixed amount of imagery containing both satellite and UAV photos of earthquake and other types of weather-caused disasters.

Despite their usefulness in post-disaster assessment, optical satellite images do have some limitations. Firstly, they only provide a single top-down view of the buildings, and are easily affected by tall vegetation that cover the roofs when seen from above. In addition, they are limited in terms of resolution, failing to provide detailed information of each individual building. Moreover, satellite images become affected by the weather conditions such as cloud coverage or extreme sunlight, as well as the time of the day and whether it is daytime or nighttime, thus obstructing a clear and uninterrupted view of the buildings. All these drawbacks are critical in the aftermath of a disaster. However, satellite images can successfully provide information regarding overall areas and regions which have been damaged, and can therefore be used for having an understanding of the most severely-struck areas.

2.1.2   SAR Imagery

To overcome limitations of satellite-based post-disaster assessment, the use of SAR imagery has been widely studied in the recent years. A synthetic aperture radar, being an active radar, creates two-dimensional or three-dimensional images from the objects. The image construction is based on the reflection of the radar received from earth and the movement of radar over a specified region, which mitigates the spatial resolution of the images, and provides stereographic reformation of the earth landscapes from space, therefore being independent from weather conditions and distances [35]. A sample SAR image has been presented in Fig. 2-3.
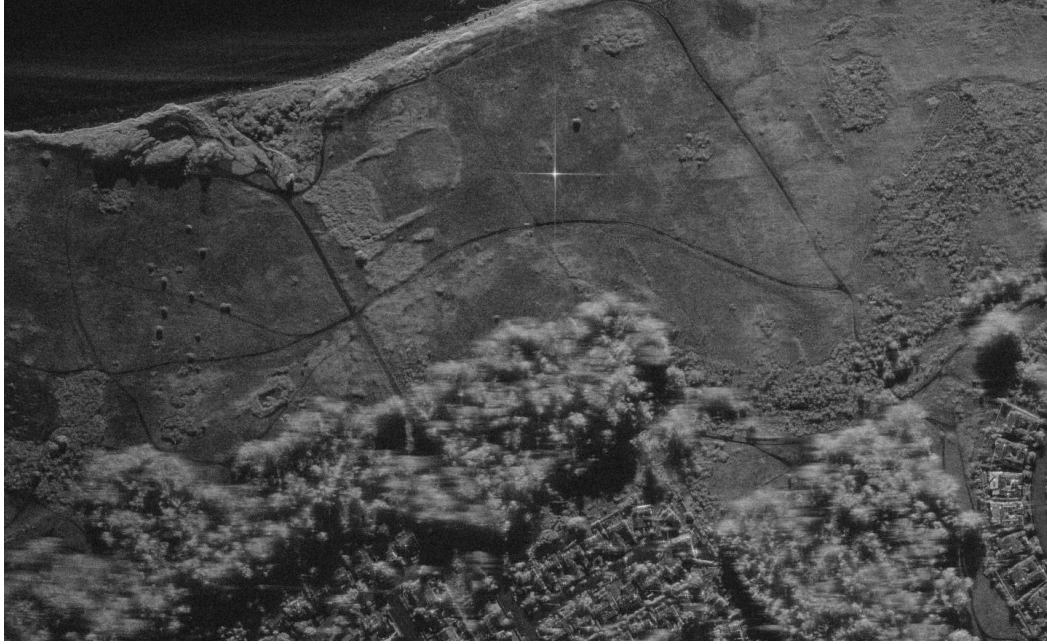
Fig. 2-3: Sample SAR image from Santa Barbara, California, US (Source: Umbra Space, under the Creative Commons Attribution 4.0 International (CC BY 4.0) license [36])

SAR imagery is accordingly functional in post-disaster assessment and damage detection of the struck regions and buildings. An application of this tool has been in near-real time flood inundation mapping [37]. The creation of post-evet flooding maps currently rely largely on both satellite and SAR imagery, along with hydraulic model simulations, as stated by Scotti et al. [38]. A study by Kosianka et al. [39] investigated the pre- and post-hurricane monitoring by analyzing the data of SAR satellites to generate historical change maps, detect the trends and conclude prominent change events such as a baseline for flood mapping following a hurricane. Some parameters such as soil moisture and ground disturbance also become investigable using specific SAR data.

In terms of more extensive damage detection after disasters, Chini et al. [40] investigated the flood mapping within urban areas. In their method which incorporated SAR imagery, the buildings were first detected and afterwards, the coherence feature of SAR data assisted in identifying the existence of flood water inside urban areas. Validated by the Hurricane Harvey data, the method

proved effective when compared with optical images. Dai et al. [41] employed the SAR images of a mountainous region in Sichuan, China to identify the damaged areas caused by Xinmo landslide. They integrated SAR data to detect stable areas and find the landslide source areas and boundaries. In addition, the tool has been effective in the creation of a precise high-resolution digital elevation model before failure, facilitating accurate estimates of the depletion and accumulation volumes of the landslide, along with the scraping area through the comparison of pre-failure and post-failure data. In another study, Saha et al. [42] proposed an unsupervised model which works based on the feature extraction of very high resolution (VHR) SAR imagery. The study aimed to detect destroyed buildings through change detection, and to achieve this outcome, it performs a pixelwise feature comparison using a convolutional neural network which is pre-trained on aerial imagery and optimized for SAR imagery. The model works effective on an earthquake-struck region in Italy.

A more recent study by Ferrentino et al. [43] harnessed multi-polarization SAR data to assess the post-quake situation by introducing an index to capture the damage level of clusters of buildings based on a decision-tree classifier. Studied over an earthquake in Italy, the method reaches an accuracy of 71 percent when considering two levels of damage for the buildings. Even though SAR imagery have been widely studied and proven to be useful, they come with a few limitations. For instance, a limited data acquisition speed [44], and more complexity when considering the data collection and analysis. In addition, the studies which have investigated the SAR imagery have focused more on regional and landscape damages, such as landslide or flood-hit regions, rather than a detailed analysis of the damage of each individual building.

2.1.3 UAV Imagery

The most recent approaches of the image-based post-disaster assessment employ UAV imagery to overcome the overall limitations of various satellite-based data. Compared to other imagery methods, UAV provides more privilege and adjustability considering that the viewing angles and elevation can be modified depending on the application. Currently, UAVs have two primary applications, including surveying and inspections [45]. The research industry has also taken advantage of the UAV abilities for damage identification. As an instance, there has been a growing use of UAVs for flood management. UAV imagery can assist in estimating flood volumetric changes in the challenging-to-access areas such as forests, which are impractical for ground surveys [46]. Additionally, Ezequiel et al. [47] employed UAV-based aerial imagery in order to facilitate the recovery process after a Typhoon, where in addition to the assessment of buildings and infrastructure, the harm to the agricultural industry and crops was also investigated. Fig. 2-4 demonstrates a sample UAV image captured in Edmonton, Alberta.

Fig. 2-4: Sample UAV image from a residential neighborhood in Edmonton, Alberta

A growing utilization of UAV imagery is also being witnessed for the damage assessment of other disaster types, including hurricanes and earthquakes. The previously-mentioned study by

Ghaffarian et al. [29] employs UAV imagery in addition to satellite imagery for assessing the debris identification. Calantropio et al. [48] incorporated the UAV photogrammetry alongside a deep learning tool as an automated building footprint segmentation and damage classifier to perform a post-disaster damage assessment, testing on an earthquake-struck region in Italy. Another research on post-earthquake situation has been carried out by Yu et al. [49]. The study focuses on the extraction of geometrical features of the buildings captured by UAV, and segments structural components based on point cloud data, which aids in the estimation of structural inclination, and residual drift estimation at story-level and system-level. Validated by two multi-story structures, the method proves to be able to estimate the deformations with high accuracy.

To provide a low-cost solution for surveys of hurricane damage in the Caribbean island of Dominica, Schaefer et al. [50] proposed a UAV-based method which compares the pre-hurricane and post-hurricane imagery, and performs an image processing method for detecting the damaged areas and geomorphological and landscape changes. Yeom et al. [51] conducted a study exploiting UAV for surveying the aftermath of Hurricane Harvey in Southeastern Texas, and employed the data for estimating the damage of buildings. The study has been based on a region growing scheme and digital elevation model, which quantifies the damage of struck buildings using the elevation change and spatial difference of the debris followed by the disaster.

Utilizing a rather different approach, Zhou et al. [52] investigated the use of LiDAR (Light Detection and Ranging) to assess the damage on roof of buildings. Based on the cluster matching of pre- and post-event imagery of various types of airborne, satellite and SAR imagery, the volume, orientation and shape of the roofs can be determined and utilized to characterize the extent of damage within each building followed by events such as hurricanes. A study by Wu et al. [53] took advantage of UAV imagery of typhoon aftermath alongside GIS tool to perform a

reconstruction of building houses and vegetation areas for different periods, and accordingly reflect the damage status of the disaster. Whitehurst et al. [54] utilized UAV imagery and Digital Elevation models to build a 3D visualization of flood events and perform segmentation over debris to assess the damage of the buildings. Another study with a focus on floods has been done by Jimenez-Jimenez et al. [55], which incorporates both satellite and UAV imagery of pre- and post-disaster situations, digital elevation model and object-based image analysis to assess and estimate the number of houses which have been completely washed away or experienced a full or partial roof collapse. The method has been validated by a river overflow situation and has proven to be accurate.

Similar to the satellite-based post-disaster damage assessment, UAV-based damage assessment has also been rendered achievable through the sole utilization of post-disaster imagery and the absence of pre-disaster data. Calton et al. [56] carried out a research that involved damage assessment of coastal hazard events such as hurricanes and floods. In their study, transferable models consisting of artificial neural networks have been examined to detect the damaged of flood and non-flood events, in the categories of damaged roofs, damaged walls, structural damage and flood damage. The previously-mentioned study by Zhang et al. [33] which focused on the image processing of post-earthquake situation, employed UAV imagery parallel to satellite imagery for the validation of their method. By way of comparison between their satellite-based and UAV-based results, they achieved a higher accuracy of 83.25 percent when using UAV imagery, proving its higher effectiveness.

Focusing on the building structures, high resolution UAV images capturing various views of buildings, such as the top-down and side perspectives, in a single shot makes them invaluable toward post-disaster assessment. To name a study that highlights the fruitfulness of having

multiple views from a single building, Khajwal et al. [12] proposed a classification based on deep multi-view image fusion. While the study does not rely solely on UAV imagery, and includes four side-view images of a building in addition to a top view (five views in total), it demonstrates the higher workability of the deep learning model when multiple views are accessible by reaching an accuracy of about 65 percent in predicting the damage category of building within five damage states. Another advantage of capturing multiple views is to facilitate a comprehensive damage assessment using a reconstructed 3D model of the building, according to this study. While it could be challenging to collect multiple views from a building in a post-disaster situation and specifically those captured from a street-view, it can be deducted that the angle seen through a UAV which consists of both top view and side views, provides more functionality and precision compared to optical satellite imagery which comprise only a single top-down view. This effect is more visible in earthquake damages, where a house might undergo a pancake collapse, meaning that the roof is seen undamaged from the top nonetheless of the whole destruction of that structure. As a result, the use of UAVs offers a more accurate approach compared to other categories of imagery.

Another upside of utilizing UAV, currently being under research, is the possibility of automatic routing within an area and neighborhood, as studied researchers such as Fu et al. [57] and Nagasawa et al. [58]. The former has studied a framework for detecting damage within distribution systems, and have validated the routing on a specific neighborhood. Meanwhile, the latter has studied the reconstruction of 3D models from damaged buildings, by prioritizing a route optimization process. The approach entails the creation of camera location points encircling specific damaged buildings, which are subsequently organized through either the K-means or Fuzzy C-means techniques. Following the clustering of camera locations and their assignment to individual UAV units, a route optimization procedure is implemented, treating it as a multiple

traveling salesman problem. The final step involves refining the paths to steer clear of obstacles, resulting in optimized routes for each UAV that strike a balance between flight distance and time. With the automated navigation and routing of the UAV, a whole urban area and the corresponding neighborhoods can be uninterruptedly covered and a real-time damage assessment can be provided.

2.2 Damage Assessment Solely through Post-disaster Imagery

The potential of conducting post-disaster assessment using both pre- and post-disaster images face a significant limitation due to the need for pre-disaster data, which may not be readily available after a disaster for all affected regions. Consequently, attention has been directed towards employing only post-disaster imagery as a primary resource. To this end, a range of image processing and Machine Learning methods have been developed for the damaged building identification employing post-disaster images. In a recent novel study, Cheng et al. [19] analyzed UAV imagery with Convolutional Neural Networks to create an effective tool for detecting and classifying building damage in hurricane-affected regions. Compared to previous aerial-imagery-based studies, their study had a deeper and more specific focus on individual buildings rather than entire regions, made possible by the high resolution UAV images. The study reaches an accuracy of 65.6 percent in localizing the buildings, and 61 percent accuracy in detecting the damage state within five damage classes. A novelty of this study is the utilization of Earth Mover's Distance as loss function, which is in fact the "minimum cost required to transform distributions to each other, functioning as a metric to assess the difference between two probability density functions" [59][19].

A challenge associated within all sorts of imagery for post-disaster assessment purpose is the recognition and detection of buildings, which is currently being addressed mainly by supervised

learning methods. Convolutional neural networks currently play an inevitable role in the object detection and within this subject, buildings are not an exception. In this regard, various studies have been done, including a study by Pi et al. [60]. Various object classes such as people, car and roofs undergo two transferable CNN-based image segmentation models in this study and as a result, the countable and bulk objects can be detected. The aforementioned study done by Cheng et al. [19] also investigates the localization of hurricane-struck buildings through the exploitation of transfer learning and CNN-based architectures.

While supervised learning methods and especially the utilization of various architectures of convolutional neural networks have proven to be effective for performing damage assessment on buildings, and have been commonly used for assessing natural disasters showing a substantial improvement, the swift implementation of supervised classification remains a challenge. This challenge is attributed to the complexity of acquiring numerous labeled samples in the aftermath of disasters [25]. As a result, the focus of current research investigating the machine learning models has been mostly on semi-supervised and unsupervised models, or supervised models which have transferability. For instance, the previously-mentioned study by Tilon et al. [34] harnessed unsupervised Generative Adversarial Network (GAN) for detecting anomalies, subsequently detecting damaged buildings in the aftermath of disasters using both satellite and UAV. In general, the GANs consist of two convolutional neural networks, which include the generator and the discriminator. The generator aims to produce data which resembles the original data, and the discriminator aims to differentiate between the original data and the data generated by generator. These two networks play a zero-sum game and the final goal is to increase the data for the underrepresented class. Even though the success of such machine learning models have been

inevitable, gaining a deeper understanding of how each feature contributes to buildings damage can lead to a more effective and less complex model developments.

A smaller portion of previous studies have shown that approaches other than machine learning are also capable of the damage assessment based on sole use of post-disaster imagery. For instance, the previously-mentioned study by Zhang et al. [33] gets advantage of the textural analysis for the post-earthquake damage detection. The study incorporates both local and global texture features. The local scale is accomplished through Local Binary Patterns (LBP) while the global features are resulted by the Gray Level Co-occurrence Matrix (GLCM). The method proposed by Ghaffarian et al. [29] which investigates the debris identification also incorporates features resulted by image processing including the aforementioned local and global texture features. In addition, the study utilizes the Histogram of Oriented Angles, which is a measurement of the orientation of the edges and aids in defining the shapes [61]. Another example of damage identification based on the texture analysis of post-disaster images is done by Joshi et al. [62], who segmented the images into uniform superpixels and harnessed multiple features from each superpixel, utilizing the method for damage identification on aerial images of earthquake-struck regions. Being less used for the post-disaster assessment purpose, another product of image processing with applications in damage detection is the edge detection. For instance, various edge detection methods are utilized for the structural health monitoring and more specifically, crack recognition within concrete structures [63]. Another instance of utilizing feature analysis alongside machine learning and neural networks is done by Ghaffarian et al. [64]. This study attempts to increase the training samples for feeding the neural networks, which is done by automatically generating them through pre-disaster building data by map tools such as OpenStreetMap. However, after producing the training patch, the damaged and demolished buildings are detected partially using their features.

More specifically, the Histogram of Oriented Angles and the Angle Density Index (quantity of angles on the edge-detected building images) are employed for this purpose. In addition, other post-disaster assessment research with less focus on buildings and larger focus on infrastructure have used texture analysis. An instance is studied by Wang et al. [65] which investigated the damage detection on roads using remote sensing imagery. After recognizing the centerline of roads, the study utilizes features such as road brightness, rectangularity and aspect ratio to create a knowledge model and detect the damaged roads accordingly.

Overall, even though being less researched, detecting damage through the image processing and feature analysis of post-disaster remote sensing images has a great potential in providing a rapid and time-efficient post-disaster damage assessment framework, since of being independent from training data and heavy computational processes. In addition, feature analysis through image processing provides deeper insight in how the image properties correlate to the damage level, therefore increasing the reliability of the models, and enabling the expandability of models and making them more efficient and less heavy in terms of computations.

2.3 Chapter Conclusion

Even though a large portion of the previous research have focused on the comparison between pre- and post-event images, the more recent studies have had a swift towards the sole utilization of post-event imagery, which not only compensates for the absence of up-to-date pre-event imagery and the mismatch between the pre- and post-event imagery, but also provides a more accelerated damage assessment framework as a fewer amount of data and images require to be processed. As a consequence of which, this study focuses solely on post-disaster imagery for the assessment. Furthermore, considering the aforementioned advantages of UAV imagery compared to its satellite counterpart, and in order to obtain higher quality images comprising more details,

more sides and views from each house and uninterrupted by weather conditions, utilizing UAV (drone) as the primary tool for the post-disaster data collection is more effective. It is however noteworthy that satellite images have the potential to be used as a preliminary damage analysis and provide information regarding the hardest hit areas, with a more detailed damage analysis related to each individual building done afterwards using the drone images.

Furthermore, despite the current progress in utilization of various supervised or unsupervised machine learning tools, having a deeper understanding of the contribution of various features tied to each house image is of significant importance. Accordingly, this study focuses more on an explicit, expandable and computationally-light damage assessment method based only on image processing. In total, this approach places a strong emphasis on the rapid and seamless damage evaluation, primarily relying on a single post-disaster UAV image for each house. Consequently, In order to fill the current gaps in literature, the study is shaped by the following conventions:

1. Sole reliance on post-disaster imagery and no reliance on pre-disaster imagery

2. Requiring only a single-view UAV image of each house

3. Utilization of Image Processing as the damage assessment tool

Depending on the literature, analysis of the texture and edges are some of the effective image-processing-based features which have the potential of detecting damage, hence being utilized in this study. The following chapter provides an in-depth description on each of the aforementioned image processing techniques and how they contribute to developing indexes for damage detection.

Chapter 3. Methodology

The method developed in this study is made up of two stages. The first stage is the Image Processing, which is in fact the tool for developing damage identifiers and the second stage is the Naïve Bayesian Classifier, which utilizes the damage identifier indices provided in the first stage as input and predicts the damage state for each building image. The outcome derived from the execution of these two procedural stages on the images manifests as a probability value delineating the likelihood of each building being damaged. Fig. 3-1 demonstrates the overall flow of the methodology in the study.

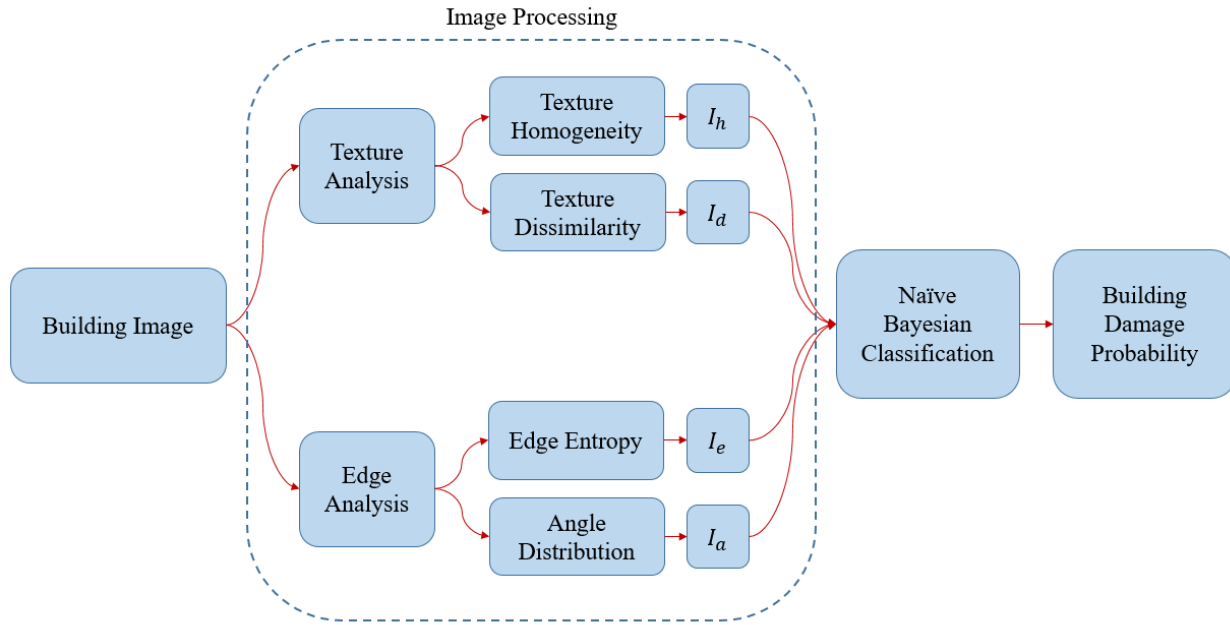**Fig. 3-1: The illustration of the methodology and the steps for reaching damage assessment**

3.1 Image Processing

In this study, a novel approach is introduced, based exclusively on image processing, for the extraction of four features related to damage detection. The methods and features utilized for detecting the damage are detailed in this section, which are divided into two subsections: texture

analysis and edge analysis. Each of the two feature analyzes result in the determination of two features which lead to identifying indices, producing four indices in total, as described in the following.

3.1.1 Texture Analysis

Texture is the overall arrangement and appearance of the pixels and their intensities inside an image. Different pixels hold different intensities. For instance, some of them are brighter and some are darker. This overall variation leads to an understanding of the damage. Two of the features essential for damage detection are extracted through the global textural analysis of images. The analysis and the features are acquired using the Gray Level Co-occurrence Matrix (GLCM) [66]. The GLCM matrix provides a statistical approach which is utilized for understanding the global textural properties of the image by quantifying the occurrence frequency of specific gray levels within a defined range in the image. When the colors within an image are disregarded and it is assumed to be grayscale, each pixel within the image has a specific level of gray, ranging from solid black to solid white, and a value defying the gray level is assigned to each of the pixels. As a result, the GLCM matrix is a square matrix with rows and columns corresponding to the gray levels, and its dimensions are equal to the total number of specified gray levels. For example, if 256 tons of gray are defined (0 denoting black and 255 denoting white), the resulted GLCM matrix will have a dimension of 256 by 256. The matrix elements are populated based on the frequency of occurrence of these gray tons in adjacent pixel pairs within the defined range in the image. In this study, the default number of gray levels (i.e. 256) is employed, and an adjacent range of 3 pixels apart is assumed for the selected pixel pairs. For illustration, Fig. 3-2 depicts an example of this matrix for a hypothetical 5 by 5 pixels image, assuming the presence of 8 gray levels and a neighborhood range of 3 pixels.
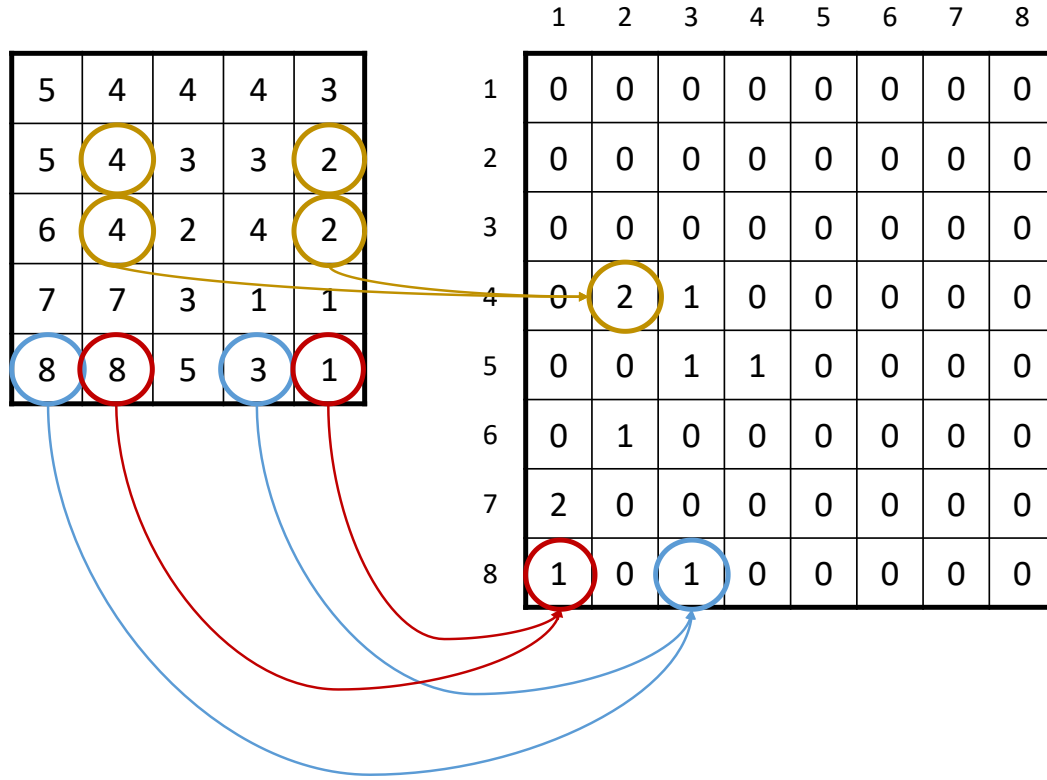
Fig. 3-2: The GLCM of an example image with 5×5 pixels

As mentioned, actual images with larger amount of pixels, alongside 256 levels of gray have been utilized in this study. Using the GLCM matrix, some features can be derived which effectively describe the global texture of an image. Previous studies, such as Zhang et al. which used the post-earthquake satellite imagery for damage assessment, have incorporated this matrix to extract features including angular second moment, homogeneity, dissimilarity, entropy and correlation for performing the post-disaster analysis [33]. In addition, this matrix and its features have been used in other fields. For example, in the area of forestry, Abdollahi et al. [67] found the high contribution of GLCM features including dissimilarity, homogeneity and the mean value of GLCM alongside image-related parameters such as hue and brightness for mapping the urban vegetation using aerial imagery. Among the various GLCM features, the study found that GLCM

dissimilarity and homogeneity values aid in differentiating the non-vegetation and vegetation areas. Meanwhile in the area of agriculture, Romano et al. [68] incorporated GLCM outcomes including parameters such as dissimilarity, contrast, entropy and uniformity (second angular moment) to evaluate the mixing of soil in organic farms. From the representative features, the dissimilarity and uniformity have shown the highest contribution levels.

The applicability of GLCM has also been investigated for the infrastructure management purpose. To assess the road condition for instance, Robet et al. [69] incorporated the homogeneity, correlation, contrast and energy features of the recognition of cracks and potholes. Daneshvari et al. [70] took advantage of GLCM outcomes to detect between the raveling and non-raveling asphalt surface, noting the contribution of contrast, dissimilarity and homogeneity in distinguishing the two classes. In terms of urban area management, Kuffer et al. [71] studied the extraction of slum areas from satellite imagery using the GLCM variance, which prove effective considering the contrast of the buildings with their surroundings. To present a final example, O'Byrne et al. [72] utilized the matrix and its derivatives to perform a semi-automated segmentation on infrastructure surfaces, identifying surface damages. The features utilized in the study include homogeneity, contrast, correlation, and angular second moment.

Relying on the literature, and considering the damage assessment purpose of the study, the GLCM derivatives employed in the study include the frequently-used dissimilarity and homogeneity. The indices I_d and I_h used for dissimilarity and homogeneity are as shown in Eqs. (1) and (2), respectively [66].

$$I_d = \sum_{i,j=1}^{N-1} \frac{1}{5} (P_{i,j} |i-j|) \tag{1}$$

$$I_h = \sum_{i,j=1}^{N-1} \frac{10 P_{i,j}}{1+(i-j)^2} \tag{2}$$

In the above equations, $P_{i,j}$ corresponds to the GLCM value of i$^{\text{th}}$ row and j$^{\text{th}}$ column. While the original equations are free of constant coefficients, in order to scale the indices in a comparative manner, a coefficient of 1/5 and 10 have been applied to the dissimilarity and homogeneity equations, respectively.

In the context of textural analysis and GLCM, dissimilarity represents the average absolute difference in the gray level intensity between pairs of pixels at a given distance and a specific angle, quantifying how different the pixel values are in the specified direction and range. A lower value of dissimilarity means that pixels near each other are closer in terms of intensity and gray ton. Homogeneity, which is also known as inverse difference moment [66], also calculates the proximity of the gray level intensity values to the diagonal of the GLCM matrix, denoting the happening of various gray levels in nearby pixels. However, it is affected more by how often the large intensity differences happen within the image, and how far the values are from the main diagonal. Homogeneity is also affected by the number of gray level tons within the image and an image with less variety of gray level values receives higher homogeneity. A lower homogeneity value means that the pixel pairs in the image have larger difference in terms of gray level value, depicting a less uniform image.

Both dissimilarity and homogeneity are sensitive to sudden and highly-different gray intensities in the image. Conversely, a parameter such as angular second moment is not affected by how different the intensities of neighboring pixels are. For example, a checkered image, where every other pixel is colored pure black and pure white (lowest and highest gray values) can be assumed, along with another checkered image with the same setting but instead of black and white, two gray levels very close in intensity value have been used for coloring every other pixels. These two images represent the same value in terms of angular second moment, unlike dissimilarity and

28

homogeneity in which the latter image scores much higher (lower dissimilarity and higher homogeneity value) compared to the former black and white one. As a result, for the damage detection purpose where abrupt and intense changes occur regionally in the building image, homogeneity and dissimilarity have been chosen as the best representative GLCM features.

To demonstrate the functionality of the indices on images, an example is provided in Fig. 3-3. In this figure, Fig. 3-3 (a) depicts a solid-colored image with a consistent gray level throughout. In Fig. 3-3 (b), the same solid-colored image incorporates narrow straight lines with a white color, while Fig. 3-3 (c) features thicker and irregular white-colored lines. From left to right, the dissimilarity index (I_d) is computed as 0, 0.96, and 1.35, respectively, demonstrating an ascending trend as the lines are introduced and the shapes become more irregular. Conversely, the homogeneity index (I_h) is calculated as 10, 9.32, and 8.55 for Fig. 3-3 (a), (b), and (c), respectively, indicating a declining pattern.

(a)   (b)   (c)
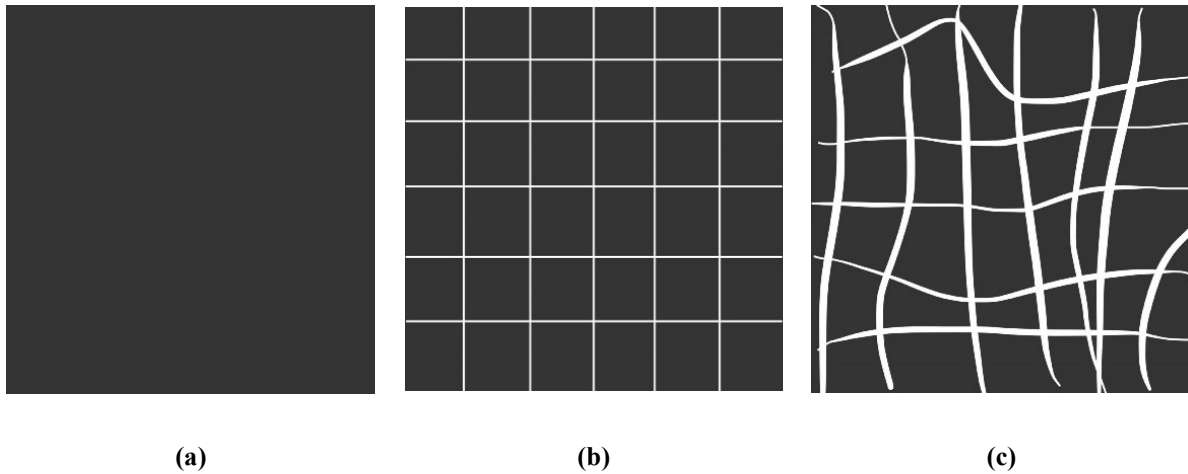
Fig. 3-3: Sample images for investigating the GLCM texture parameters of dissimilarity and homogeneity

Since increased abrupt fluctuations are anticipated in the gray level of pixels within the image of damaged buildings, an increase in the level of dissimilarity and a corresponding decrease in the level of homogeneity are expected. To illustrate this, an example of an undamaged building (Fig. 3-4 (a)) and an example of a damaged building (Fig. 3-4 (b)) are presented and their resulted feature

values have been compared. The calculated dissimilarity values are 1.52 and 3.82 for the undamaged and damaged scenarios, respectively. Additionally, the homogeneity values are determined as 1.88 and 1.04 for the respective cases. As expected, the undamaged building incorporates a higher homogeneity and a lower dissimilarity value.

(a)   (b)

Fig. 3-4: Sample image of (a) an undamaged building captured using drone in an Edmonton neighborhood and (b) a damaged building captured by drone after a hurricane in Tennessee, USA [73]

3.1.2   Edge Analysis

Although the texture analysis will provide promising differences between undamaged and damaged images, it is prone to certain constraints. An example is the architectural design of the building which may significantly affect the patterns observed in the images, which in turn alters the textural elements, especially considering that the focus of study is specifically on the buildings. Therefore, this study proposes incorporating edge-based analysis to complement the texture-based features.

In a broader context, edge denotes the points within an image where an abrupt and significant alteration occurs in the brightness level, primarily signifying object boundaries. An edge-detected representation of and image is a visual depiction that highlights the boundaries and transitions

between distinct objects or regions within the image. An edge-detected image simplifies the image processing by eliminating the unnecessary data of the image while maintaining the important structural patterns and features related to the boundaries [74], which are useful for identifying damage as the boundary patterns tend to change compared to when damage is nonexistent. Edge detection has been used in the monitoring of structures and civil infrastructure systems, as employed by Gül et al. [75], studying the edge detection of videos captured by cameras to assess the lubrication level of open gears in movable bridges.

The specialized image processing technique of edge detection is achieved through algorithms like Canny edge detection [74]. The capabilities of Canny edge detection method have been widely explored across various domains. For instance, in the biomedical field, Ze et al. [76] harnessed the Canny edge detector to segment blood vessels in specific image types. The applicability of Canny edge detection has also been majorly researched on various forms of object detection. An example is done by Chung et al. [77] for detecting highway accidents. The method combines an object detection tool, along with Canny edge algorithm, which aids in the detection of accidents and compensates for the low amount of database. It has also been useful in detecting moving objects, as researched by Zhan et al. [78], where Canny edge detection has complemented a frame-difference-based algorithm for detecting the objects through continuous frames. In this case, the aid of the Canny edge is in achieving the edge difference image to compare the number of non-zero pixels for detecting the moving parts. In the area of civil and structures, the method has been employed for identifying cracks in concrete bridges, such as an study by Abdel-Qader et al. [79]. The study reached a high accuracy utilizing Canny edge detector and concluded that the Canny method resulted the second highest accuracy among the other employed methods. Other studies focused on the crack identification of infrastructure using the Canny edge detection have been

frequently carried out. For instance, Han et al. [80] utilized Canny edge method alongside Decision Tree to detect cracks on highway pavements, and concluded the success of Canny edge method in crack detection and its helpfulness in obtaining more details of the crack areas in comparison to other edge detection methods. Another example which is applicable on metal structures has been studied by Wang et al. [81], who investigated the workability of Canny edge method on detecting internal cracks within infrared images. The method which involves a three-step thresholding has been applied on pipe surfaces.

Canny edge detection is a technique with computational approach specifically designed to enhance edge detection accuracy by systematically analyzing the intensity variations in pixel values across an image, with the primary goal of pinpointing abrupt changes that typically signify object boundaries or significant features. The method follows three main criteria [74]: The first concern is achieving a low error rate to ensure that edges in an image are accurately detected without missing any and without generating false responses. The second critical criterion is the precise localization of edge points. This involves minimizing the distance between the points identified by the detector and the central position of the actual edge. This localization is especially crucial in applications like stereo and shape from motion, where small disparities are measured between left and right images or images captured at slightly different times. However, since the first two criteria would not be adequate for creating smooth edges, Canny method recognizes a third criterion to prevent the occurrence of multiple responses to a single edge. Optimal operators for ridge and roof edges are derived through numerical optimization. The criteria are further tailored for step edges, and a parametric closed form for the solution is provided. To achieve the desired outcome of solid and smooth edges while maintaining a light computational procedure and

fulfilling the three mentioned criteria of detection, localization and single response, the Canny edge method consists of the following steps [74][82].

Initially, the grayscale image is subjected to noise reduction, leading to the production of a smoother image. Typically, this operation involves the application of a Gaussian kernel to convolve the image. Subsequently, the calculation of the image gradient is performed based on the intensity variations of gray levels, yielding both gradient magnitude and the orientation and angle information [82]. Following this, a non-maxima suppression process is implemented to eliminate spurious edge thickness, resulting in edge thinning. More specifically, for each of the pixels in the gradient direction of the edges, only the pixel with the highest gradient magnitude within the neighborhood is maintained and the other less significant pixels are suppressed. The fourth stage involves double thresholding, where pixels possessing robust intensity levels are retained as edges while those with insufficient intensity levels are discarded. The step involves two threshold limits, including the upper threshold and lower threshold. The threshold values for this phase can be adjusted to control and fine-tune the inclusion or exclusion of edges within the image. The pixels which demonstrate a higher gradient magnitude than the upper threshold limit are considered as strong edges, hence kept in the detection. Meanwhile, the pixels demonstrating a low gradient magnitude below the lower threshold limit are not considered edges and therefore, eliminated. The pixels falling in between these threshold limits are not considered strong edges, but are maintained in case they are connected to strong pixels and belong to a solid edge, a process which leads to the fifth and final step, where a hysteresis-based edge tracking method is employed to eliminate the weak pixels that do not correspond to well-defined and definitive edges.

Fig. 3-5 provides an illustration of the results obtained using the Canny edge method for the identical samples of undamaged and damaged buildings previously shown in Fig. 3-5, utilizing the default values for the gradient kernel size and gradient calculation.
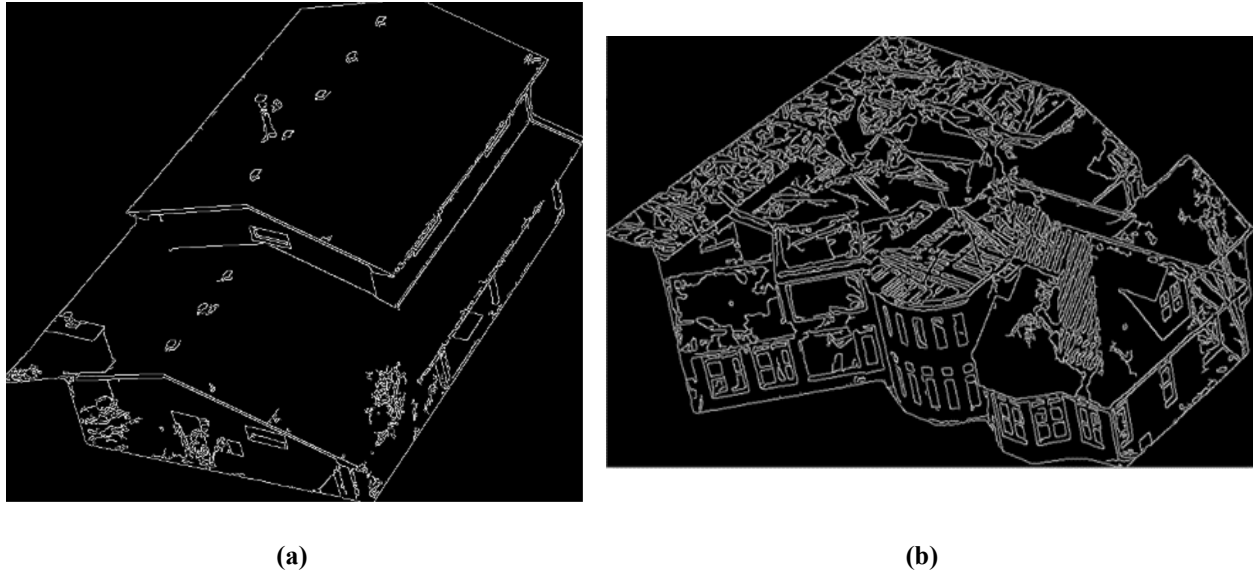

<div align="center">(a)   (b)</div>

Fig. 3-5: Edge-detected images of (a) the undamaged case and (b) the damaged case shown in Fig. 3-4

As mentioned previously, the threshold limits of the Canny edge detection can be chosen to desire, and in this study, the lower limit is adjusted in order to account for the inconsistency of the image sizes and prevent the detection of unnecessary edges within images with very high resolutions, while keeping the important edges within images having lower resolutions. In order to keep the results as consistent as possible, a fixed value has been chosen for the upper threshold value, as it is very determinative in the edge-detection result and all the edges with higher intensities are kept. Therefore, changing it unprecedentedly alters the edge detection result. However, adjusting the lower threshold limit has less effect in the result and comes advantageous in preventing the over-detection of edges. In an intensity range between 0 to 255 (0 corresponding to pure black and the minimum intensity magnitude, and 255 corresponding to pure white and the maximum intensity magnitude), a constant upper threshold of 200 is implemented, meaning that

the pixels with an intensity higher than 200 in the aforementioned scale are selected as edges, while the lower threshold is adaptively adjusted based on image quality. Specifically, for images with higher resolutions, where a greater number of edges are identified, the lower threshold value is increased in accordance with Eq. (3). This adjustment aligns the edge detection outcomes between high-resolution and low-resolution images, ensuring consistency in edge detection across various image types. For the majority of images, the lower threshold value is constrained within the range of approximately 60 to 100. The values 60 and 100 are chosen according to the suggestion for Canny method, which mentions the method works better when the ratio between the lower threshold and upper threshold is kept in the range of 1 to 2 and 1 to 3 [74].

Lower threshold limit:

$$\frac{image\ size}{1000} * 0.08 + 10 \tag{3}$$

Fig. 3-6 illustrates an example of applying different values of lower threshold limit, showing how the result of edge detection would be affected. In this figure, (a) presents the original image comprising an undamaged building with a rather high resolution, which has been captured by a drone in the Edmonton area. Meanwhile, (b) presents the Canny edge detection when the limit from Eq. (3) is applied (equal to 99 in this very case), while (b) and (c) present the edge-detected image when the lower threshold limit of 60 and 10 have been applied, respectively. As it could be observed, adjusting the lower threshold limit results in the exclusion of unnecessary patterns and inclusion of the definitive patterns.
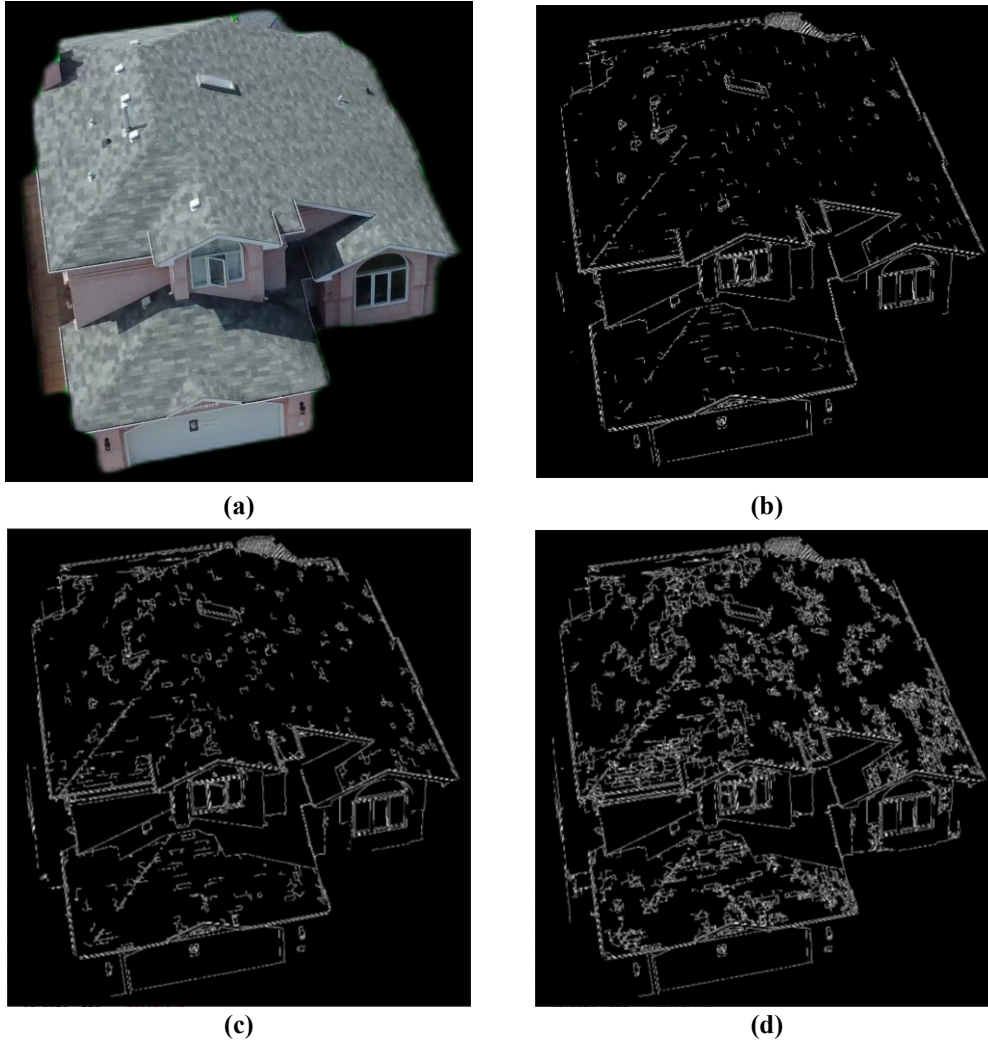
Fig. 3-6: Sample Canny edge-detected images for the building presented in (a) applying various lower threshold values of (b) 99, (c) 60, and (d) 10

Following the application of the lower threshold limit, all Canny-detected images are uniformly resized by employing the interpolation resizing techniques. This step is motivated by the fact that the analysis outcomes of the edges are closely linked to the resolution of the edge-detected image. By standardizing the image size while maintaining the ratio between the length and height of the image, the negative impact of database inconsistencies can be mitigated. The scaled edge-detected images are then utilized for extracting two other features which are further described.

3.1.2.1   Edge Entropy

The first edge-based feature utilized for damage detection in the study is the entropy of the edges. To achieve this, the Shannon's Entropy method [83] is applied to the Canny edge-detected images. Shannon's Entropy is fundamentally employed to gauge the prevailing uncertainty within the potential outcomes of an event, and in the context of this study, it accounts for the randomness and uncertainty associated with each potential outcome within the edge-detected image. The index used in this study is defined in accordance with the fundamental definition of Shannon's Entropy, yielding Eq. (4):

$$I_e = -\sum_{i=1}^{N} P(x_i) \log_2 P(x_i) \tag{4}$$

in which P denotes the likelihood and x_i corresponds to the outcome of each pixel.

Developed in 1948 for application in information theory, the equation for Shannon's entropy (Eq. (4)) defines how unpredictable an event could be [83]. An example can be described with an event which has two possible outcomes, such as a coin toss. The lowest entropy is achieved when only one of the two outcomes happens all the time, for example when the coin always lands on the heads and never lands on tails, in which case the entropy would be calculated as zero. Meanwhile, the highest entropy is achieved when the coin toss is in complete fair condition, and there is a 50 percent chance of landing on either of heads or tails. In other words, in a fair coin toss, the result is in the most unpredictable state possible. The same scenario happens on the Canny edge-detected images, as performed in this study. The functionality of Shannon's Entropy in structural health monitoring and its potential in detecting damage within signal processing of civil infrastructure has been studied, with an interesting example of which being the research on damage identification in truss structures done by Moreno-Gomez et al. [84]. In this study, the damage associated with corrosion in truss bridges has been analyzed using the vibration signals generated at various

conditions, and Shannon's entropy has been one of the utilized tools for analyzing the signals. Another study is carried out by Amezquita-Sanchez et al. [85] which evaluates various entropy-based methods, including the Shannon's entropy, for damage detection in the high-rise buildings exposed to dynamic vibrations through the analysis of their vibrational response recorded by sensors and accelerometers. The study concludes the efficiency of Shannon's entropy among other methods in nonlinear measurement for damage detection.

As shown in Fig. 3-5, the Canny edge-detected images encompass two sets of pixels: black pixels, representing non-edges, and white pixels, representing edges. Consequently, each pixel within the edge-detected image can be regarded as a system with two potential outcomes. Thus, the base of 2 is incorporated for the logarithm in Eq. (4). As a result, Shannon's Entropy calculates entropy based on the probabilities associated with black/white pixel outcomes. However, the probability of each pixel being black or white is not 50 percent in the Canny edge images. In fact, in damaged building images where a more abundant amount of edge pixels have been detected, there is a higher possibility of receiving an edge pixel compared to the images of undamaged buildings where the edges are fewer. Consequently, $P(x_i)$ is higher in an image showing damaged state. Higher entropy value hence signifies a greater degree of uncertainty about the edges and a larger possibility of having multiple and random edges, implying a potential association with a building exhibiting more damage. Conversely, an image characterized by fewer and more uniform edges exhibits a lower level of randomness, leading to a diminished entropy value.

For the Canny edge images featured in Fig. 3-5, the entropy index value derived from Eq. (4) is computed as 0.78 and 3.26 for the undamaged and damaged cases, respectively, reaffirming the expectation of a higher entropy value in the presence of building damage. Since a random pixel in

the damaged case image is more likely to be an edge pixel compared to the undamaged case image, the resulted entropy outcome is higher.

3.1.2.2   *Angle Distribution of the Lines*

The second edge-based index introduced in this study revolves around the orientation of edge lines and their distribution. To perform this analysis, the initial step involves the identification of lines within the edge-detected image. For achieving this, the Hough Line transform [86] is employed. This method which is applicable on the Canny edge detected image, relies on a vote-counting mechanism to detect lines and operates within a parameter space defined by slope (m) and intercept (c), with each data point represented by a unique (m, c) pair. Each (m, c) pair is in fact a representor of a distinguished line in the system. For every edge pixel (x, y) within the Canny edge-detected image, the general equation relating slope and intercept, namely $y = mx + c$, is established, and a vote is registered for each (m, c) pair that satisfies the equation. Subsequently, the (m, c) pairs with the highest local vote counts are selected, with each pair corresponding to a distinct line characterized by a specific slope and intercept. As a result, the approximate lines forming the edge-detected image can be identified. The results of the Hough Line transform for the images featured in Fig. 3-3 (b) and Fig. 3-3 (c) are depicted in Fig. 3-7 (a) and Fig. 3-7 (b), respectively.
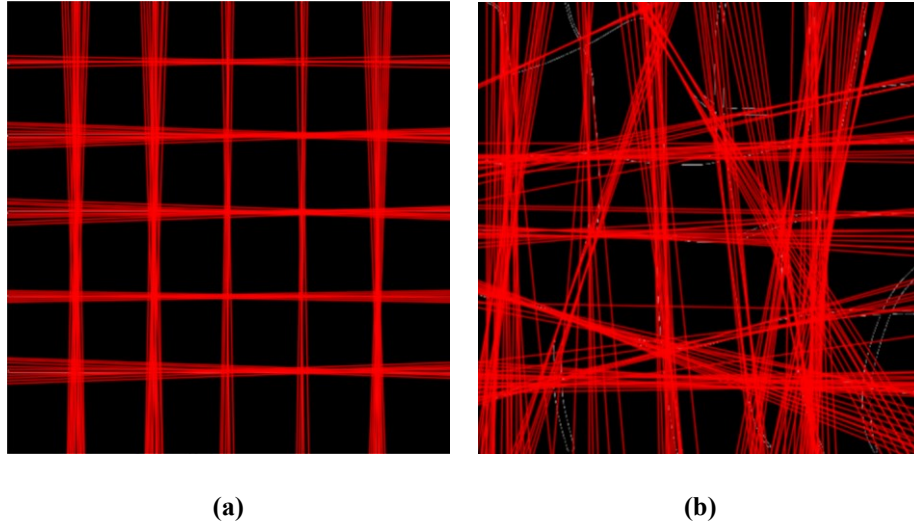
(a)   **(b)**

Fig. 3-7: Hough Line transform of sample images presented in (a) Fig. 3-3 (b) and (b) Fig. 3-3 (c)

One of the previous studies which has incorporated the angle of lines in post-disaster situation, as mentioned in the literature review, is done by Ghaffarian et al. [29], who utilized the histogram of oriented angles for debris detection. While the method of histogram of oriented angles is utilized for understanding the local patterns in the image, this intention of this study is to incorporate a global index related to the angles and orientations of the patterns to identify damaged buildings. Accordingly, the Hough Line transform is utilized instead. Hough Line transform has been previously employed for the monitoring of the structures and infrastructure. One utilization for example has been in the wind turbines, as researched by Stokkeland et al. [87], who used the Hough line transform on Canny edge detected images captured by UAV from the wind turbine. The Hough line here has been specifically used for detecting the tower and blades on turbine, aiding in the tracking process for the inspection purpose. Another study which utilizes the Canny edge and Hough line transform for data analysis of the turbine Wind Power Curves is carried out by Long et al. [88]. In this study the line transform is intended to detect the outliers on the power curve produced by the turbines. Furthermore, an interesting study to mention has been carried out by Tschopp et al. [89] for localization and high-quality positioning of the railway infrastructure.

For this purpose, the Hough transform has been used alongside sensors to construct a map resembling the railway network with high accuracy. Other instances of utilization of Hough Line transform include a study by Li et al. [90], who have utilized the line transform for UAV-based surveillance of the electrical infrastructure. The specific utilization of Hough transform in this case is for the detection of straight lines for the final intention of power line recognition. Even though there has been a noticeable amount of research employing Hough line transform for infrastructure monitoring purpose, the method has not been a focus for post-disaster assessment studies, which is despite the potential of using lines for damage detection. As a result, in this study the method has been investigated and an index has been built based on the angles of the lines detected on the image.

In the first step, the Canny edge images undergo the Hough Line transform for the lines to be detected on the building. After the lines and their associated slopes have been obtained through the Hough Line transform, an analysis of angle distribution within the range of 0 to 180 degrees and with a precision of 1 degree is conducted. The expectation is that undamaged buildings tend to display well-organized lines with angles that are consistent and closely aligned with each other, while damaged buildings typically exhibit chaotic gradients in various directions and incorporate a wide variety of angle ranges. To assess the degree of angle disorganization, the density histogram of these angles is compared to a uniform distribution. As a result, a closer alignment of the histogram with a uniform distribution indicates a higher level of angle disorganization, signifying an increased likelihood of detecting a damaged building. Conversely, a histogram featuring sharp peaks and deep troughs suggests that the angle orientations are concentrated at specific points (degrees), indicative of a building with less damage. In order to be assessable and comparable, the angle distribution histograms have been formed in 5-degree slots for both undamaged and damaged

cases, as presented in Fig. 3-4. The undamaged and damaged case presented in Fig. 3-4 (a) and (b), are illustrated in Fig. 3-8 (a) and (b), respectively. Additionally, a red line representing the uniform distribution is overlaid on the histograms for reference. A histogram where the bars are closer to the uniform line indicates the existence of orientations in all different angles, depicting a chaotic and probably damaged image. As demonstrated in Fig. 3-8, the undamaged case sees a larger concentration of lines in specific angle ranges around 20, 40, 80 and 100 degrees, and there is quite an absence within 120 to 180 degree angles, while the damaged case conversely does not have a specific concentration and lines are present in many different angles.
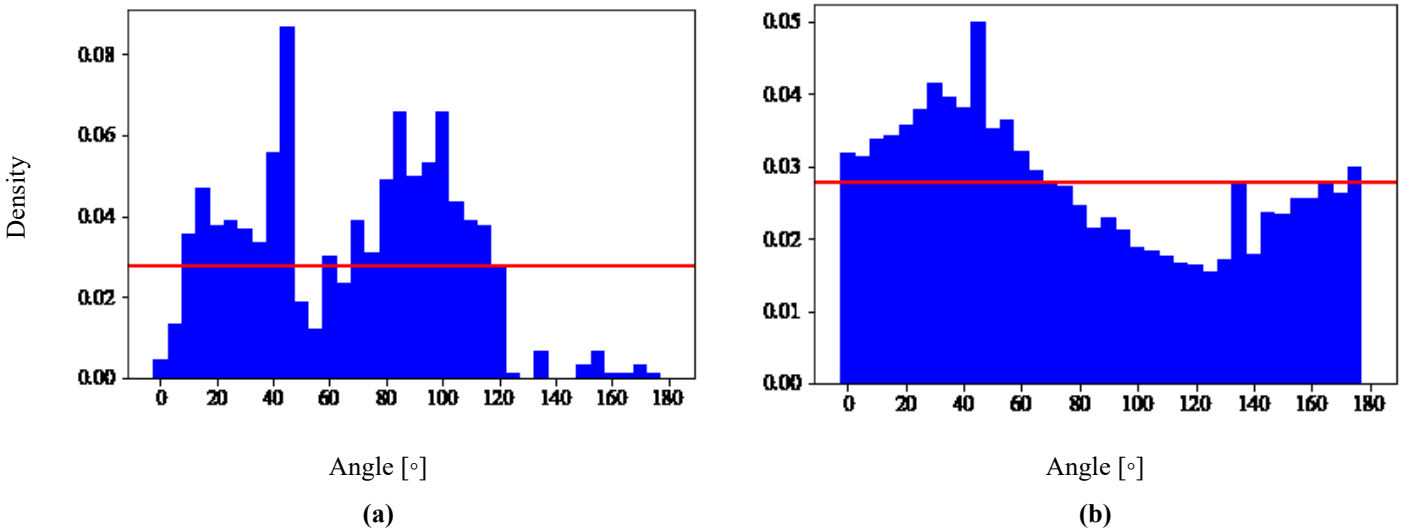
Fig. 3-8: The angle density histogram of (a) the undamaged and (b) the damaged case shown in Fig. 3-4

The index defined in this section is based on the comparison of angle distribution and uniform distribution of the histogram, achieved through the Root Mean Square Deviation (RMSD) function. To scale the results, a natural logarithm is applied on the RMSD value as shown in Eq. (5):

$$I_a = ln(1000\sqrt{\sum \frac{(x_i-\mu)^2}{n}})$$

(5)

where x_i represents the data points within the obtained distribution, μ denotes the probability density function (PDF) value corresponding to the uniform distribution, and n represents the total number of data points. The coefficient of 1000 is employed to scale the index and render it comparable with other indexes. Since the bars in a histogram with sharper peaks and deeper troughs tend to have a larger difference with the uniform distribution, the index is expected to be calculated higher for undamaged case histograms. The I_a values for the histograms featured in Fig. 3-8 (a) and (b) are calculated as 3.13 and 2.10, respectively, with the higher value observed in the undamaged case.

As a result, four distinct damage identification indices have been delineated. These indices are subsequently deployed in the computation of the structural damage classification of the building under consideration, leading to the next section describing the classification method and the subsequent calculations.

3.2 Classification

In this study, Naïve Bayesian classification technique is employed to account for the classification of damage category based on the image-based features explained in the previous section. The basis of Naïve Bayesian classification is rooted in Bayes' theorem, which is expressed as follows:

$$P(c|X) = \frac{P(X \mid c)P(c)}{P(X)} \tag{6}$$

where $P(c \mid X)$ is the posterior probability of class c given the observations in vector X, $P(X \mid c)$ is the likelihood function showing the probability of observations in X given the class of c, $P(c)$ is the prior probability of class c, and $P(X)$ is the prior probability of the observations. Assuming the independence of the features, Eq. (6) can be rewritten as:

$$P(c|X) = \frac{P(x_1 \mid c)P(x_2 \mid c)P(x_3 \mid c)...P(x_n \mid c)P(c)}{P(X)} \qquad (7)$$

The four predictor parameters of angle index (I_a), entropy index (I_e), dissimilarity index (I_d), and homogeneity index (I_h) which have been defined in this study, are assumed to be independent. This is an assumption made for the simplicity, as the as the indices are not completely independent in the context of extracting image properties. Consequently, Eq. (7) for this study is shaped as below:

$$P(c|I) = \frac{P(I_a \mid c)P(I_e \mid c)P(I_d \mid c)P(I_h \mid c)P(c)}{P(I)} \qquad (8)$$

Considering the two damage classes of this study, namely damaged and undamaged classes, Eq. (8) is translated to the following two equations:

$$P(U|I) = \frac{P(I_a \mid U)P(I_e \mid U)P(I_d \mid U)P(I_h \mid U)P(U)}{P(I)} \qquad (9)$$

$$P(D|I) = \frac{P(I_a \mid D)P(I_e \mid D)P(I_d \mid D)P(I_h \mid D)P(D)}{P(I)} \qquad (10)$$

The likelihood functions for each feature described in Eq. (9) and Eq. (10) can be derived by creating a class-specific database, forming the subsequent density histograms of the indices for each of the two classes, and fitting an appropriate probability distribution to the histograms. A dataset comprising 202 undamaged and 113 damaged building images (a total of 315 images) has been utilized in this study. Exemplary undamaged and damaged images were presented in Fig. 3-4 of the preceding section. For the testing purpose, at each validation step 15 images are randomly selected out for testing, and the rest of the 300 images are used for creating the probability distribution functions which is further described in the results section. Furthermore, the prior probabilities for each class were computed based on the respective class percentages within the database, resulting in 64.1% for the undamaged class or $P(U)$ and 35.9% for the damaged class or

$P(D)$. The final component in Eq. (9) and Eq. (10), denoted as $P(I)$, represents the prior probability of the observations, and can be opened up as follows:

$$P(I) = P(I_a)P(I_e)P(I_d)P(I_h) \qquad (11)$$

In Eq. (11), $P(I_x)$ is in fact the probability of the feature disregarding the undamaged or damaged class. In other words, it is the probability density of that specific number for the feature when both classes are combined and there is only one distribution for all the classes gathered. For all the four indices, this amount is the same for both the $P(D|I)$ and $P(U|I)$, thus canceled out during the computation of posterior probabilities for the damaged and undamaged classes, since it appears in the denominator of both equations and these classes represent two complimentary events with the following relationship:

$$P(D|\mathbf{I}) + P(U|\mathbf{I}) = 1 \qquad (12)$$

Accordingly, for each set of new observations of an unknown image, the variables of $P(U|\mathbf{I})$ and $P(D|\mathbf{I})$ are calculated using Eq. (9) and (10) respectively in terms of $P(\mathbf{I})$ and afterwards, Eq. (12) is employed for calculating the probability of being on damaged or damaged category.

To reach the estimated likelihood function for each of the predictor parameters, a normal distribution is fitted to density histogram of each parameter for each of the damaged and undamaged classes separately, as presented in Fig. 3-9, all the 315 images in database have been used to create the histograms and graphs. Considering that the histograms represent a shape close to normal distribution, and having the expectation that a larger database further contributes to reaching a normal shape, normal curves have been chosen as the best fitted distribution to the histograms. Afterwards, the features and predictor values of unknown buildings i.e. the images selected randomly for testing are extracted, and by employing the distribution functions, the

posterior probability of the damage observed in that building is calculated through Eqs. (8), (10) and (12).
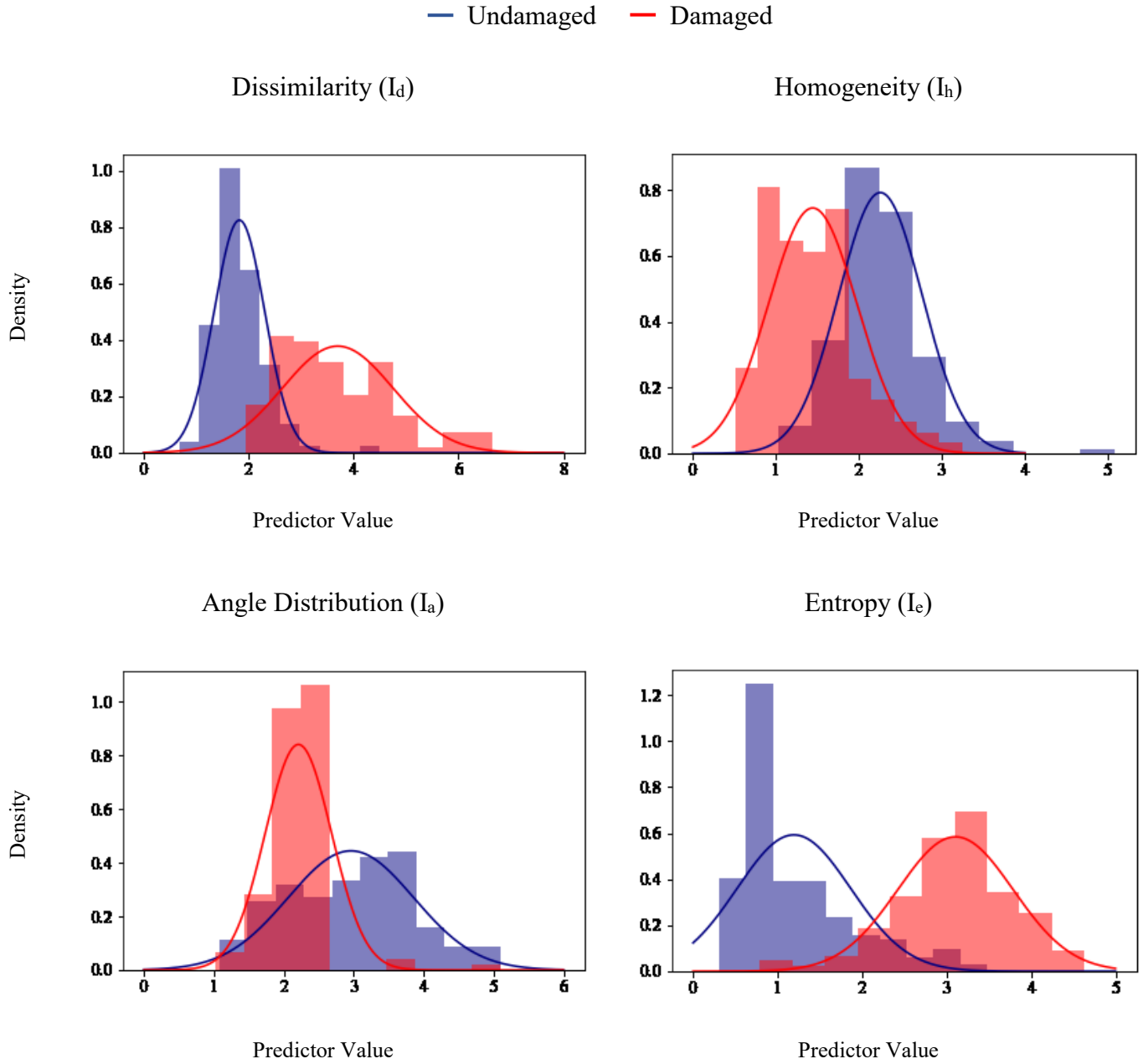

Fig. 3-9: Estimation of likelihood distributions for predicting parameters of I_d, I_h, I_a and I_e

From the graphs presented in Fig. 3-9, it could be seen that the normal distribution is a compliant fitting likelihood distribution function for each case. Since the likelihood distributions

are all probability density functions, the area under all the curves is equal to one. Consequently, each of $P\ (I_x|U)$ and $P\ (I_x|D)$ phrases in Eq. (9) and (10) could be translated to the probability of feature x in the subsequent normal distribution of the feature in each of the damaged and undamaged cases. Since the damage is to be identified using the indices, and the value of these indices are a representor of the image rather than a direct identification of the inherent damage, a continuous distribution function would be acceptable. However, it is noteworthy that the damage itself, when investigated inherently, is a rather discrete phenomenon. Considering that the focus of this study is to identify overall damage level, and considering the use of indices, a continuous distribution can be utilized as a proper estimation.

In the following, an example has been provided to illustrate the calculation process for providing a deeper understanding of how different index values contribute to the damage classes, and determining whether the case belongs to the damaged or undamaged category. For this purpose, the undamaged house presented in Fig. 3-10 has been utilized. It is expected that at the end of the calculation, the building has a very low probability of being damaged.

Fig. 3-10: A sample undamaged building captured by drone in Edmonton area

The feature indices of Fig. 3-10 are calculated accordingly as:

Angle Distribution: $I_a = 3.53$

Texture Dissimilarity: $I_d = 1.96$

Edge Entropy: $I_e = 0.93$

Texture Homogeneity: $I_h = 1.86$

Having the indicating parameters, $P(I_x \mid D)$ and $P(I_x \mid U)$ are calculated for each features using the normal density distribution graphs from Fig. 3-9. The red curves are utilized for calculating $P(I_x \mid D)$, and the blue curves are utilized for calculating $P(I_x \mid U)$:

Angle Distribution ($I_a = 3.53$):
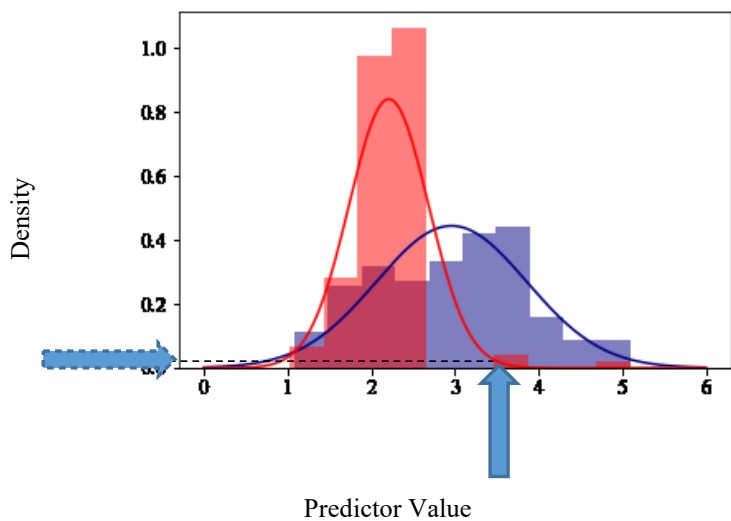
$P(I_a \mid D) = {\sim}0.04$ $P(I_a \mid U) = {\sim}0.35$
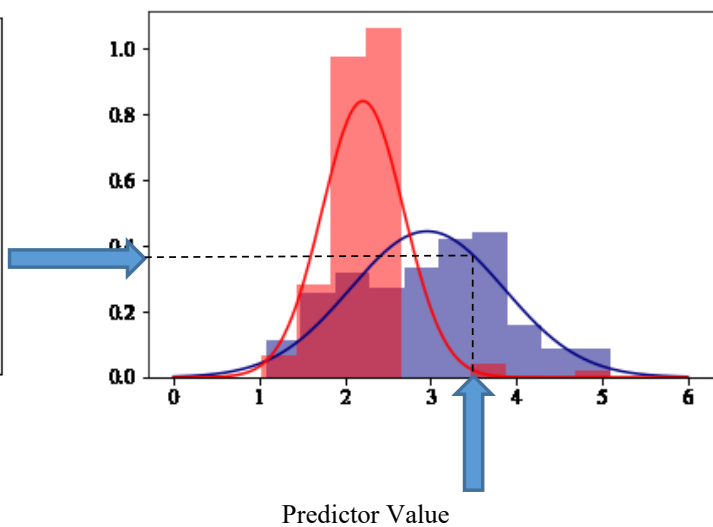
(a)

Texture Dissimilarity ($I_d = 1.96$):
$P(I_d \mid D) = {\sim}0.12$ $P(I_d \mid U) = {\sim}0.75$

(b)

49
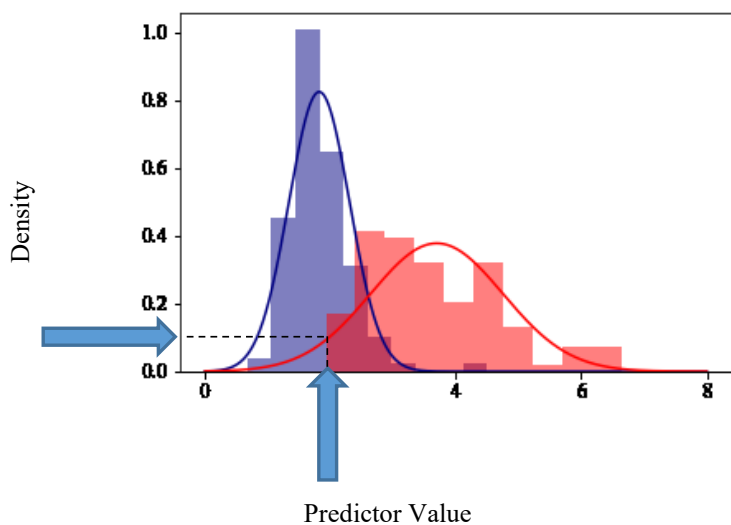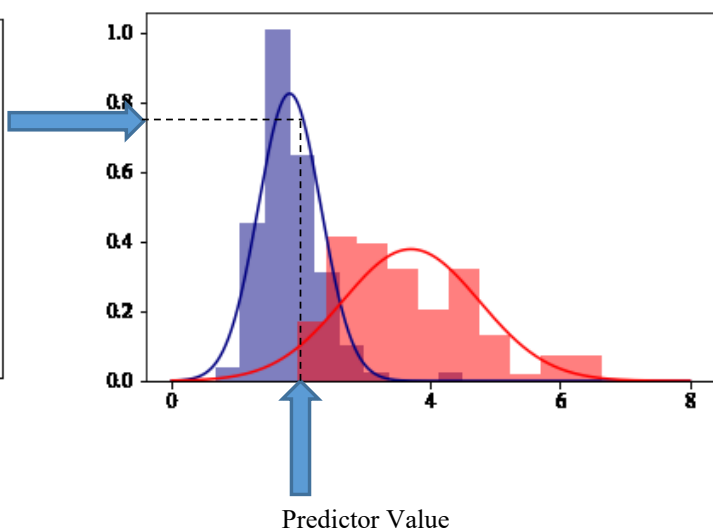
Edge Entropy ($I_e = 0.93$):
$$P(I_e \mid D) = \sim 0.02$$
$$P(I_e \mid U) = \sim 0.55$$
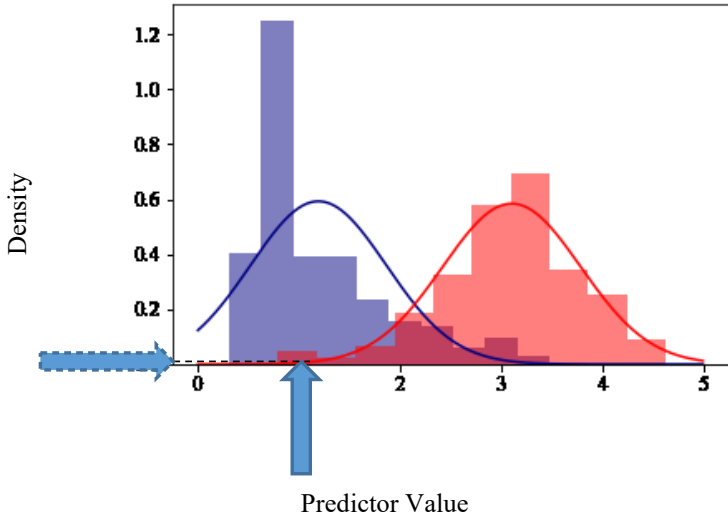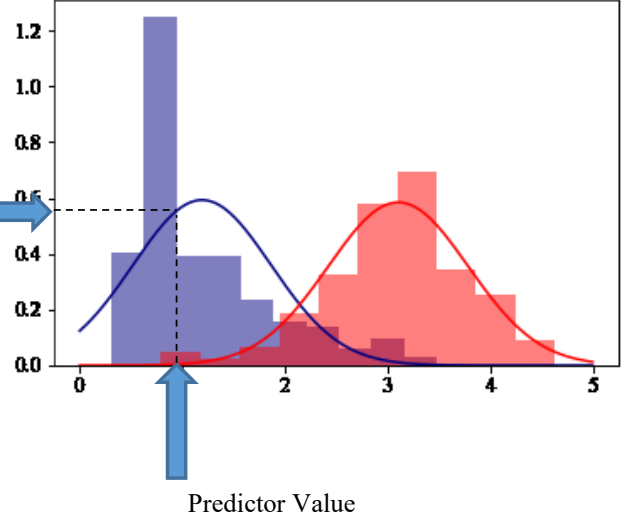
(c)

Texture Homogeneity ($I_h = 1.86$):
$$P(I_h \mid D) = \sim 0.55$$
$$P(I_h \mid U) = \sim 0.65$$
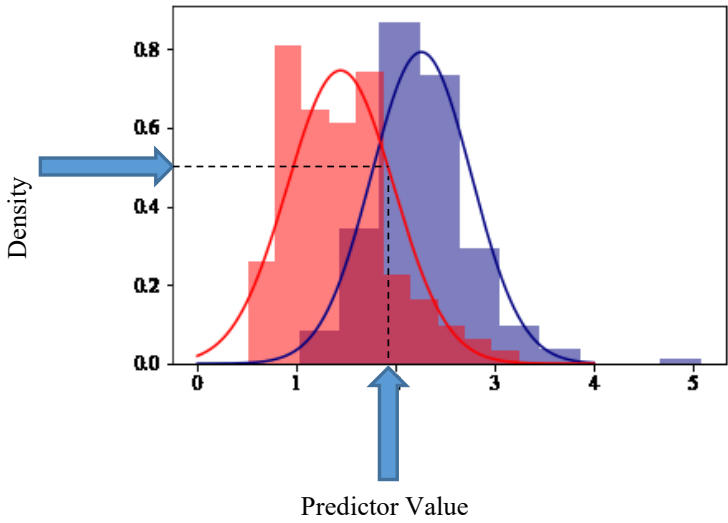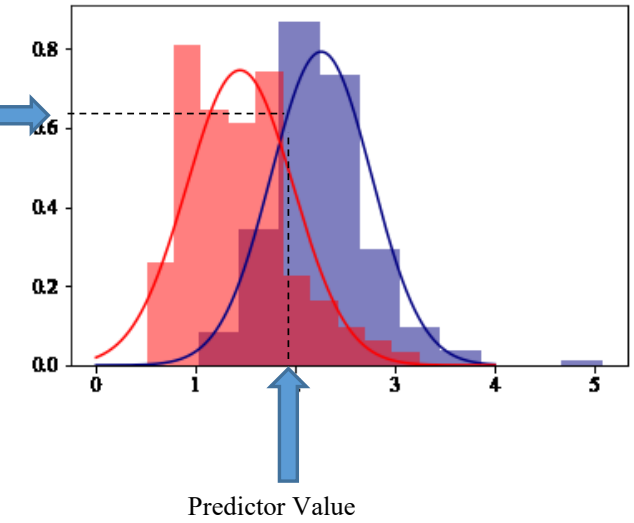
(d)

Fig. 3-11: Finding the probability density value for the parameters of (a) angle distribution, (b) texture dissimilarity, (c) edge entropy and (d) texture homogeneity calculated for the image in Fig. 3-9

Utilizing the approximate probability values calculated from the graphs thorough Fig. 3-11 inside Eq. (9) and Eq. (10), and considering the ratio of damaged and undamaged cases provided

for creating the graphs (113 damaged and 202 undamaged), $P(D|I)$ and $P(U|I)$ are calculated as follows:

$$P(D|I) = \frac{0.04 \ \times 0.12 \times 0.02 \times 0.55 \times 113/315}{P(I)} = \frac{1.9\,e - 5}{P(I)}$$

$$P(U|I) = \frac{0.35 \times 0.75 \times 0.55 \times 0.65 \times 202/315}{P(I)} = \frac{0.06018}{P(I)} = \frac{6018\,e - 5}{P(I)}$$

Finally, employing Eq. (12) and considering $P(U|I) + P(D|I) = 1$, the final probability of being damaged can be calculated accordingly:

$$\frac{P(D|I)}{P(D|I) + P(U|I)} = \frac{1.9}{1.9 + 6018} = \%0.03$$

$$\frac{P(U|I)}{P(D|I) + P(U|I)} = \frac{6018}{1.9 + 6018} = \%99.7$$

The calculation concludes that the building has a very low chance (0.03 percent) of belonging to the damaged category, classifying it as undamaged. Having a closer look at the predictor values, it is evident that for this specific case the homogeneity feature is the least determinative in terms of yielding an undamaged result, as the predictor value for undamaged and damaged case is very close (0.65 vs. 0.55). Meanwhile, the edge entropy contributes most to the result, as the difference within the undamaged and damaged predictor values is very high (0.55 vs 0.02). However, when blended with each other, the effect of less-contributing parameters would be neglected. The case is not the same for other images, as for some of them the texture parameters have higher contribution to the result compared to the edge parameters, signifying the importance of utilizing all four indicators together.

The Naïve Bayesian Classification as a result provides a transparent and computationally-light method to classify the buildings according to their damage level. The method has been already applied for various purposes in the engineering field. A prominent instance is in the monitoring of

pipeline system, and detecting the failures and breaks in the pipes [91][92]. While the method has not been researched as much for the post-disaster situations, the transparency and quickness blends well with the provided image processing techniques for building a rapid post-disaster assessment tool.

3.3 Chapter Conclusion

The method of this study is based on the texture-based and edge-based image processing of building images, and for each image, 4 identifying indices are built upon the result of analyzes. These identifiers include texture dissimilarity, texture homogeneity, edge entropy and the distribution of line angles. The damage classification is performed using a Naïve Bayesian Classifier, which intakes the 4 subsequent identifiers, with an assumption of their independence, and outputs the probability of being damaged with a percentage value, ranging from 0 to 100. To perform this, the probability density functions for each of the indices are constructed according to a database of undamaged and damaged buildings. Consequently, each building is categorized as either damaged or undamaged. The functionality of this model, and its application on real-life instances is further described in the following chapter.

Chapter 4. Results and Discussion

In this section, the functionality of this post-disaster assessment model would become evident. In the beginning, the database which has been utilized for assessing the model has been described in more details, followed by a preliminary application of the model on the database to provide a deeper look into the functionality of the model. The model is then undergone a testing examination using unseen database (images which have not been used for creating graphs), and finally, a real-life application on the model has been demonstrated.

4.1 Database Preparation

As described in the previous section, the database employed in the study consists of 202 undamaged and 113 damaged building images. While a smaller portion of the undamaged images utilized in the study are sourced from the internet, the majority have been captured by a drone through the larger Edmonton area, and from various neighborhoods within the city. Fig. 4-1 depicts the image of the drones utilized in the study. The drones include a DJI Mini 2, and a DJI Phantom 4.

The elevation of drone during the data collection has been approximately 30 meters from ground. The camera had an approximate pitch angle of about 40 degrees, whereas the yaw and roll angles have been zero. An illustration of the three axes and their corresponding rotation angles is presented in Fig. 4-2. This angle position theoretically means that the camera has a forward vision, but instead of looking directly straight, it is tilted 40 degrees towards down (ground). The combination of flying elevation and camera angle should be selected wisely, as it should enable an inclusive and multi-sided view of the buildings. In other words, a sufficient proportion of each of the buildings' roof and facades should be visible in the images.

(a) **(b)**

Fig. 4-1: The image of the drones utilized for data collection: (a) DJI Phantom 4 and (b) DJI Mini 2
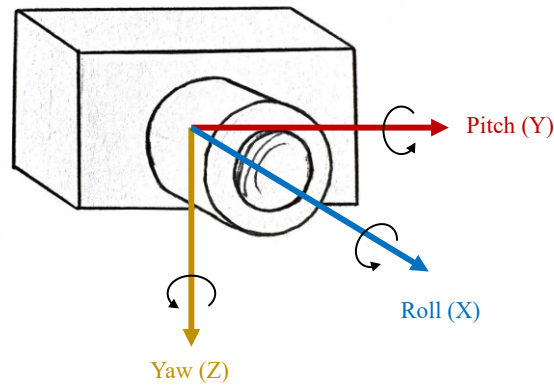
Fig. 4-2: The demonstration of Yaw, Pitch and Roll axes in the camera

Sample drone images captured in two various neighborhoods of the city can be found in Fig. 4-3 (a) and (b). The location of this neighborhoods is shown in Fig. 4-4. The damaged database however is sourced completely through internet, mostly comprising of buildings damaged by hurricanes and, with a lesser extent, earthquakes. A sample drone image from a region hit by hurricane (storm) which is utilized in the database of this study has been presented in Fig. 4-3 (c).

(a)

(b)

(c)

Fig. 4-3: Sample drone images utilized for preparing the database
(a): An image captured in the neighborhood of Castle Downs in northwest Edmonton
(b): An image captured in neighborhoods south of University of Alberta Farm
(c): An image showing post-storm damages in Chattanooga, Tennessee, US in April 2020 [73]
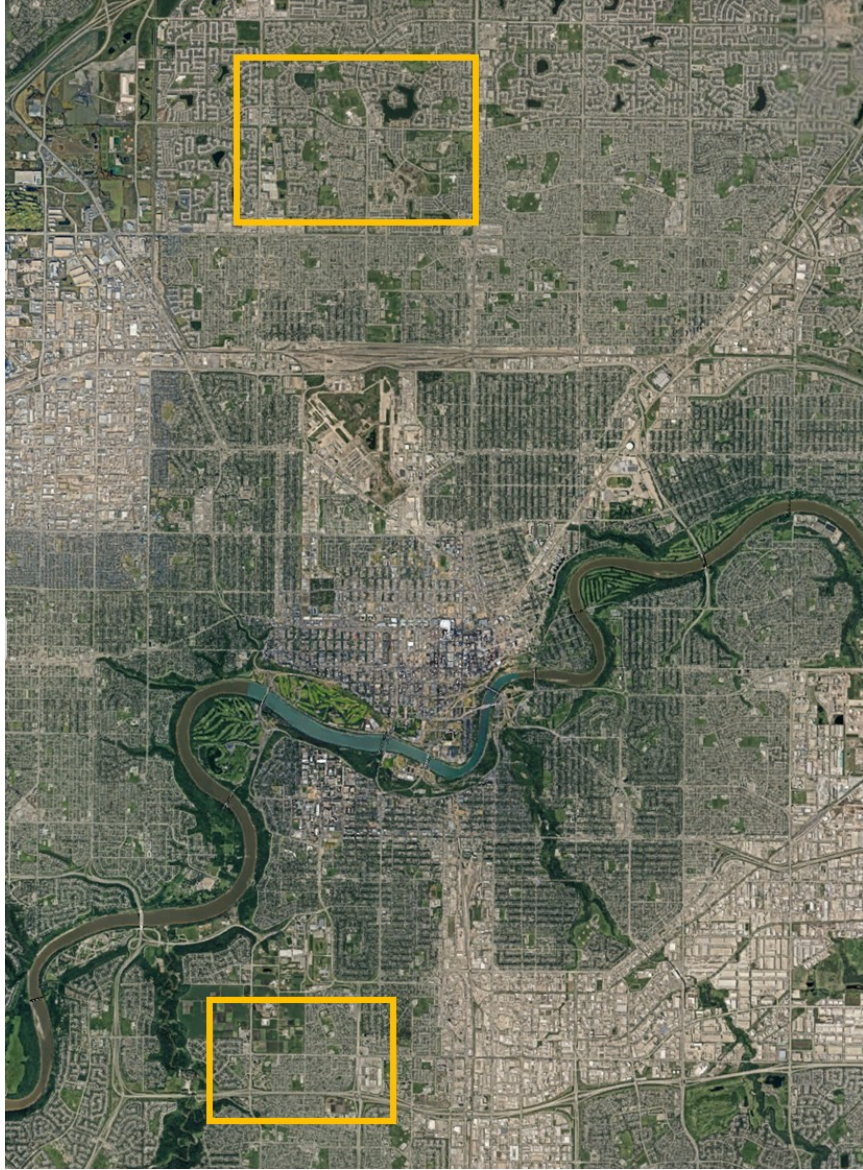
Fig. 4-4: A map of Edmonton showing the approximate locations where the data has been collected, taken from Google Maps [93]**. The northern location shows the neighborhood of Fig. 4-3 (a) and the southern neighborhood shows the neighborhood of Fig. 4-3 (b)**

4.2   Functionality of the Proposed Framework

This step which is incorporated mainly for the investigation purpose rather than testing, involves all the 315 building images being fed to the model. The initial result is the probability density functions as presented in Fig. 3-9 in the previous section. In these graphs, the shape of the histograms closely resemble a normal distribution for each of the cases as they are aligned with

the fitted normal curves. More notably, the distributions for undamaged and damaged cases are clearly distinguishable from one another. Consequently, it can be inferred that the four selected features contribute significantly to the damage level of buildings.

The Naïve Bayesian classification method is applied to categorize all the images into either the "Undamaged" class (with a probability of being damaged below 50 percent) or the "Damaged" class (with a probability of being damaged exceeding 50 percent), with the intention of assessing the feasibility of the proposed framework. The result of analyzing the 202 undamaged and 113 damaged images and predicting the damage state using the graphs in Fig. 3-9 (assuming there is no unseen sample) would be as follows:

16 undamaged buildings misclassified as damaged (accuracy: % 92.1)

6 damaged buildings misclassified as undamaged (accuracy: % 94.7)

22 misclassified buildings overall (accuracy: % 93.0)

The method as a result functions successfully in the absence of unseen data. Before running the model with unseen sets of database to test the accuracy, a number of cases are presented to further identify the underlying reason in achieving wrong results. Fig. 4-5 (a), (b) and (c) present three misclassified undamaged cases while Fig. 4-5 (d), (e) and (f) present three correctly-classified undamaged cases for comparison. All the images are captured by drone in the Edmonton area.

$P(D|I) = \%98.5$

(a)

$P(D|I) = \%65.0$

(b)

$P(D|I) = \%66.6$

(c)

$P(D|I) = \%0.6$

(d)

$P(D|I) = \%0.1$

(e)

$P(D|I) = \%0.1$

(f)

Fig. 4-5: Sample drone images from houses in Edmonton area, with (a), (b) and (c) being misclassified as damaged and (d), (e) and (f) being correctly classified as undamaged

In Fig. 4-5, the probability of being damaged ($P(D|I)$) for each of the cases has been included on the figure. For images (a), (b) and (c), one underlying reason in the incorrect detection is that the roof texture of the buildings is quite rough, resulting in the exaggerated detection of edges. Consequently, the edge-based parameters do not contribute well to the damage classification. Meanwhile, for (b) and (c), the texture dissimilarity and homogeneity are rather on the verge of transition between undamaged and damaged curves mostly due to the roof texture and are therefore unable to compensate for the negative edge contribution. In case (a) however, due to the presence of more details such as the terrace rail which constantly changes from black to white, even the texture features contribute negatively to the damage classification. Meanwhile, case (f), despite exhibiting large amount of details, is not misclassified as the texture contrast is not as striking as case (a). For case (b), the large size of the building might be seen as a source for the misclassification. However, when compared to case (e) which is also large in size, it would become evident that the size is not the source of error for this very case. The plants and trees could be observed as a minor source of the error for cases (a) and (c). Despite that, case (d) shows the result is not majorly affected by this phenomenon as the building has been detected undamaged despite the tree covering a portion of the roof and façade.

A suggested method for overcoming some of the mentioned shortcomings, such as ragged roof patterns, is the local texture analysis on the images. In contrast to GLCM which provides global texture-related features, a local texture and pattern recognition can help in understanding whether a frequent texture change is consistent or disorderly. A consistent change in the pattern is more likely to present a building component (such as roof) rather than damage.

4.3 Testing Result

While in the previous subsection the model was analyzed by inputting all the images and avoiding the unseen data, it is necessary to evaluate the performance of the model in the event of encountering new data not previously used in creating the probability density functions. The same classes of "Undamaged" (with a probability of being damaged below 50 percent) and "Damaged" (with a probability of being damaged exceeding 50 percent) are employed to assess the proposed framework in this step. To perform this assessment and ensuring the feasibility of the model, a cross-validation method is employed [94]. In this resampling-based approach, distinct subsets of data are designated for testing purposes, while the remaining data are employed for model training across multiple iterations. In the current investigation, a total of 10 iterations are utilized for model validation. In each iteration, 15 random images are selected from the complete database for testing, leaving 300 images for training and the derivation of probabilistic distribution functions. Subsequently, accuracy is computed for the undamaged subset, the damaged subset, and the entire set of 15 images in each iteration. The cumulative validation results are as shown in Table 4-1.

Table 4-1: The cross-validation results of the database using the method

	Val. No. 1	Val. No. 2	Val. No. 3	Val. No. 4	Val. No. 5	Val. No. 6	Val. No. 7	Val. No. 8	Val. No. 9	Val. No. 10
Undamaged Accuracy (%)	88.9	81.8	100.0	100.0	70.0	100.0	88.9	100.0	75.0	88.9
Damaged Accuracy (%)	100.0	100.0	85.7	83.3	100.0	100.0	83.3	100.0	100.0	100.0
Overall accuracy (%)	93.3	86.7	93.3	93.3	80.0	100.0	86.7	100.0	86.7	93.3

Overall accuracy: % 91.3

As delineated in the table, the overall accuracy stands at 91.3 percent. Although this exhibits a marginal decrease compared to the 93 percent accuracy computed in the previous phase wherein the entire database was utilized for model training, it is noteworthy that the validation accuracy remains considerably high. This outcome serves as a proof attesting to the robust functionality and practical utility of the model. While certain measures have been taken in order to account for the inconsistency of the database used in the study, by having a more consistent database with image resolutions closer to each other, a rise in the overall accuracy can be expected. This is due to the fact that the damaged images utilized in this study have been in general lower in resolution compared to undamaged images. Considering that some edges and lines are left undetected in lower-resolution images, while they can be correctly captured in higher-resolution images, higher-resolution damaged images are likely to have more accurate classifications based on the edge-based parameters. However, the texture-related parameters are less likely to experience significant changes.

4.4 Real-life Application

In addition to testing the framework through the cross-validation, the method has been applied directly on a whole disaster scene to further demonstrate its functionality. Fig. 4-6 presents a closer view of the same image of hurricane-hit Tennessee village presented in Fig. 4-3 (c), along with the marking of buildings selected for investigating the application in a disaster scene. In this image, 6 of the houses have been selected for testing the method, labelled C1 to C6. Cases C1, C2, C3 and C4 have frequent damaged parts with C4 being the least damaged one, while C5 and C6 are barely damaged. Even though some of these buildings have been used in the previous steps for the training and validation, in this very step they are not used for training and thus, appear as

unseen data to be analyzed. Since all the 6 cases utilized in this step are sourced from the same image, the effect of the inconsistency of the analyzed data and their corresponding resolution is minimized.

Fig. 4-6: The image presented in Fig. 4-3 (c) showing post-storm damages in Chattanooga, Tennessee, US and the 6 buildings selected for analysis

The damage analysis results of the selected cases is presented in Table 4-2, while the detailed index values on the corresponding probability density graphs have been presented in Fig. 4-7. In this figure, the probability of belonging to each category according to each index value ($P(I_x \mid D)$ and $P(I_x \mid U)$) can be approximated.

Table 4-2. The damage assessment result of select houses from Fig. 4-6

Category	Label	House Image	$P(D\|I)$ Using Texture only (%)	$P(D\|I)$ Using Edge only (%)	$P(D\|I)$ Using All Features (%)
	C1		100	83.9	**100**
	C2		99.9	62.2	**100**
Damaged	C3		99.7	63.9	**99.9**
	C4		82.8	14.4	**59.8**

C5		55.5	4.2	**9.0**
Undamaged				
C6		51.6	20.0	**32.9**
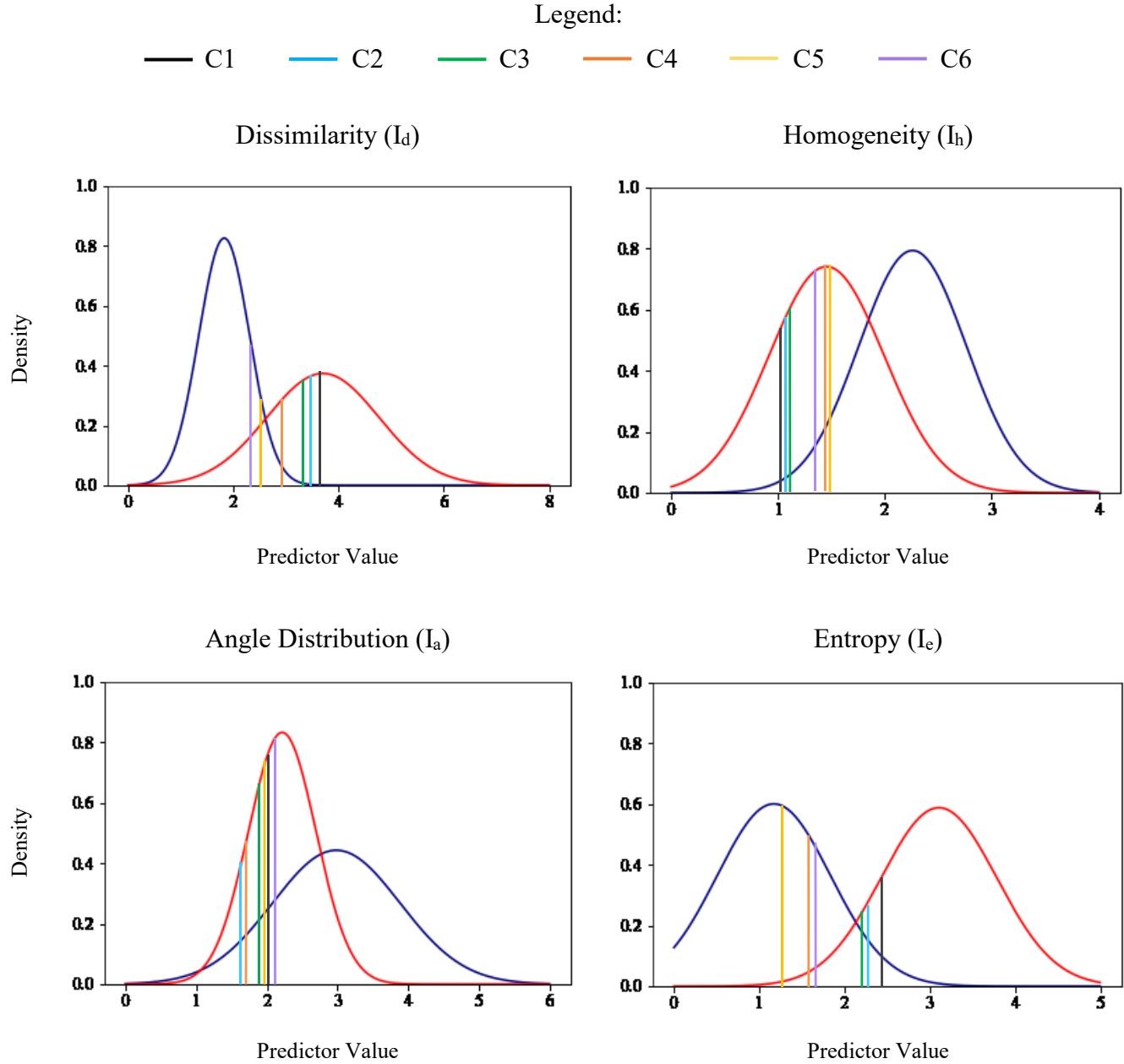
Fig. 4-7: The predictor values for each of the six cases selected in Fig. 4-6, illustrated on the probability density function graphs

According to the results in Table 4-2, when all the 4 features are used for the analysis, all the damaged and undamaged cases are identified correctly. However, when employing solely the texture features (dissimilarity and homogeneity) or solely the edge features (angle distribution and edge entropy), the same conclusion cannot be made as some cases are not identified correctly.

Even though the results might be partially accurate when each of the texture or edge features are used solo (for example C4, C5 and C6 receiving less damage probabilities than C1, C2 and C3), there overall result is not acceptable as there would be cases that do not fall in the correct damage state category. This emphasizes that the texture-based and edge-based features complement each other, thus being important to consider both of them in damage detection.

According to Fig. 4-7, for these specific cases, the angle distribution parameter is not effective for determining the overall damage level, which is mainly due to the fact that even the less damaged cases (C5 and C6) have minor breakages and cracks along with partial tree cover, showing the limitation related to the condition of images. Meanwhile, the texture dissimilarity and edge entropy demonstrate the highest contribution to the overall damage state.

In addition, the damage probability result for C4 is lower than C1, C2 and C3, which complies with the fact that C4 is not as severely damaged as the other damaged houses. Even though the detection of moderately-damaged houses has not been a scope of this study, this result suggests that the method has the potential of identifying a more specific level of damage for each building should the database expand consistently.

4.5   Chapter Conclusion

The database and data collection method for the study have been described in the chapter, and some of the correctly- and incorrectly-identified drone-captured cases have been further investigated. A fundamental reason for the incorrect classification of the selected undamaged cases is the rough texture of the roofs, which deteriorates the result of image processing. Furthermore, the images have undergone a cross-validation for testing the method, yielding a high accuracy of 91.3 percent. An analysis over a hurricane-struck region also been done to demonstrate the

applicability of the method. All the selected houses in this example could be classified accurately,

and the contribution level of each parameter to the overall damage state has been illustrated.

Chapter 5. Conclusion

5.1 Outcomes and Achievements

A novel framework is proposed in this study for the post-disaster detection of damaged residential houses, employing image processing techniques exclusively on single post-disaster UAV imagery of the houses. A high overall validation accuracy of 91.3 percent for distinguishing undamaged and damaged houses is achieved by the method. Moreover, the framework correctly detects the damage state of all the selected houses in a real-life post-disaster situation captured by UAV, with damage probabilities that are consistent according to the damage severity. The real-life application example is a proof that the method has the potential to flawlessly recognize damage in a post-disaster situation. Furthermore, this approach is characterized by computational simplicity, enabling expeditious assessment. Such property not only provides a rapid and time-efficient assessment framework without requiring an enormous amount of data to be trained, but also enables the further expansion of the model to include more disaster types. Notably, the utilization of UAV images permits the observation of multiple building views, such as top view and side views, obviating the necessity for capturing multiple perspectives. In addition, there is no requirement for the pre-disaster imagery as the framework does not function based on the comparison and rather on the irregularity of the images themselves. Hence, the assessment can be performed using only a single post-disaster UAV image of each building, further reducing the computational costs. Development of such framework has been possible through the utilization of UAV imagery.

The simplicity and transparency of the model facilitate prospective modifications, with the ease of adding or removing features and indices. These augmented features can enhance the learning process of Machine Learning models, resulting in expedited and refined model

performance. Moreover, the method allows for searching the source of error in each building. The source of error might include either or some of the texture dissimilarity, homogeneity, edge entropy or angle distribution.

This model, at its current state, is specifically utilizable for detecting the damage state of houses. When implemented on a basis where post-disaster UAV images have been collected and the houses are detected, this method has the ability to recognize the houses which have been damaged and in order to be put in direct use for a specific region or city, a larger database for ensuring the accurate workability of the model would be required. While this model has the potential to provide damage in a wider range of buildings, the main focus has been on low-rise residential houses. Furthermore, it is noteworthy that the model has been mainly developed based on damages resulted by weather-induced events including hurricanes. Earthquake damage usually comes with debris which deter the texture and edge feature of images, and a small portion of the damaged database comes from post-earthquake scenes, which suggests the ability of the model for predicting earthquake damage as well. However, ensuring this requires more study including earthquake-related damages.

5.2 Limitations

The most prominent limitation of the study arises from the database, most significantly in terms of inconsistency. Even though the study has accounted for such inconsistency by updating the threshold values and edge image sizes, a database where the images are characterized by more consistent qualities and resolutions leads to a better functionality and classification of the framework. One solution would be to capture the damaged building database by utilizing the same instrument (drone) utilized for capturing undamaged buildings to maintain the same resolution, in case a considerable number of disaster-hit houses are available and in reach. In addition, a

consistent increase in the quantity of the training data could possibly lead to more accurate probability density functions, with a closer resemblance of the actual normal curves that describe the feature. The real-life application example in this study suggests that a consistent and close-conditioned database has the potential to provide better performance and higher accuracy for the framework.

Although UAV imagery possesses advantages in terms of fewer limitations compared to alternative remote-sensing modalities like satellite imagery, it is not entirely immune to external factors, notably intense sunlight. The consequence of excessive sunlight manifests as certain sections of buildings are obscured by dark shadows, while others exhibit high exposure. Nevertheless, this limitation, while noteworthy, is not of paramount significance as substantial proportions of the majority of buildings retain reasonable visibility. In contrast to optical satellite imagery, which is sensitive to a broader range of weather conditions, including cloud cover, UAV imagery holds a comparative advantage and demonstrates an upper-hand in overcoming such challenges.

5.3 Future Research

For future research, the most important step is the inclusion of a more diverse image database with consistent and close-conditioned post-disaster images. As previously mentioned, a database with matching resolutions could possibly yield even higher accuracies. Additionally, the framework has the potential for detecting other disaster types. While the framework of this study mainly functions based on data from hurricanes, a larger participation of disasters such as earthquakes, and also an addition of disasters such as wildfires can expand the applicability of the model. Furthermore, potential expansion of classification categories, such as partially damaged, becomes feasible with a more extensive database of damaged buildings. As presented in the real-

life application, the model has the capability of detecting partial damages from severe damages in case of exposure to vaster and more consistent database.

While testing on a real post-disaster database of a specific region can aid in having a higher assurance of applicability, further expansion of the methodology could result in better applicability results. For example, utilizing local texture and pattern analysis to identify rough building sections (such as roofs) and distinguish them from damages. In addition, localizing the damages of the buildings is achievable through local texture analysis, meaning that the damaged part of the buildings (for example roof or façade wall) can be identified. Such expansion of the methodology can be advantageous in terms of the overall damage analysis result and yield higher accuracies, and meanwhile, it can be beneficial if used after the initial damage detection as a tool for a more precise localization. The overall methodology also has the potential of being applied on a wider variety of tools, such as Virtual Reality, to aid the experts in a more specific and detailed damage recognition within structures, such as the bridges.

Other areas of expansion consist of the steps towards reaching a fully-automated post-disaster assessment tool. More specifically, the first step to reach a complete framework is the automated navigation of UAV. In the wake of a disaster, the damage assessment should be immediately commenced and the drones should start the data collection by capturing aerial images and videos from the neighborhoods and regions within urban areas. In order to create a fully automated framework, various drones should be assigned to different regions, and each should have the ability to automatically survey within their corresponding neighborhoods. To achieve this, each drone is required to be programmed in a way to route above the neighborhoods, and navigate above the streets and roads, until reaching a full coverage of each region and capturing every existing building. Having the map of each region, and by following every path, such outcome can be

achieved. UAV automation is essential in order to cover every residential block within neighborhoods, while the houses remain in the clear sight of the instrument. This means that the instrument should fly in a specific route and with specific camera angles which enable a clear multi-sided view of the houses. The second crucial step is the building detection and localization. Following the full coverage of the neighborhoods and by having the post-disaster images and/or videos ready, the next step is to detect the buildings and houses, select them out from the frames and localize them according to the positioning of the drone. This step is essential for automatically selecting out buildings from the larger images and videos find the accurate location of each on the map. Ultimately, the full automation of UAVs, combined with automated building detection and image extraction, can culminate in the development of a comprehensive and seamless post-disaster assessment tool. Together with these two steps, a cutting-edge rapid post-disaster assessment technology would be within reach.

References

[1]   A. Colbert, "A Force of Nature: Hurricanes in a Changing Climate," 2022.
        https://climate.nasa.gov/news/3184/a-force-of-nature-hurricanes-in-a-changing-climate/

[2]   A. Grinsted, P. Ditlevsen, and J. H. Christensen, "Normalized US Hurricane Damage
        Estimates Using Area of Total Destruction, 1900−2018," *Proc. Natl. Acad. Sci. U. S. A.*,
        vol. 116, no. 48, pp. 23942–23946, Nov. 2019.
        doi: 10.1073/PNAS.1912277116/SUPPL_FILE/PNAS.1912277116.SD01.XLS

[3]   B. Weltman, "Severe Weather in 2022 Caused $3.1 Billion in Insured Damage -- making it
        the 3rd Worst Year for Insured Damage in Canadian History," 2023.
        https://www.ibc.ca/news-insights/news/severe-weather-in-2022-caused-3-1-billion-in-
        insured-damage-making-it-the-3rd-worst-year-for-insured-damage-in-canadian-history

[4]   T. C. Press, "The 10 Most Expensive Natural Disasters in Canada by Insurance Payouts,"
        2023.
        https://toronto.citynews.ca/2023/01/18/the-10-most-expensive-natural-disasters-in-canada-
        by-insurance-payouts/

[5]   B. Weltman, "Severe Weather in 2021 Caused $2.1 Billion in Insured Damage," 2022.
        https://www.ibc.ca/news-insights/news/severe-weather-in-2021-caused-2-1-billion-in-
        insured-damage

[6]   D. J. Frame, M. F. Wehner, I. Noy, and S. M. Rosier, "The Economic Costs of Hurricane
        Harvey Attributable to Climate Change," *Clim. Change*, vol. 160, no. 2, pp. 271–281, 2020,
        doi: 10.1007/s10584-020-02692-8

[7]   C. Aid, "Counting The Cost 2022: A Year of Climate Breakdown," 2022.
        doi: 20.500.12592/kxq66g

[8]   T. R. Knutson *et al.*, "Tropical Cyclones and Climate Change," *Nat. Geosci.*, vol. 3, no. 3, pp. 157–163, 2010.

doi: 10.1038/ngeo779

[9]   W. Commons, "Morning after Hurricane Maria." https://commons.wikimedia.org/wiki/File:Morning_after_Hurricane_Maria_(3737272146 5).jpg

[10]   Y. Kajitani, S. E. Chang, and H. Tatano, "Economic Impacts of the 2011 Tohoku-oki Earthquake and Tsunami," *Earthq. Spectra*, vol. 29, no. SUPPL.1, Mar. 2013.

doi: 10.1193/1.4000108/ASSET/IMAGES/LARGE/10.1193_1.4000108-FIG11.JPEG.

[11]   D. Kang and Y. J. Cha, "Autonomous UAVs for Structural Health Monitoring Using Deep Learning and an Ultrasonic Beacon System with Geo-Tagging," *Comput. Civ. Infrastruct. Eng.*, vol. 33, no. 10, pp. 885–902, 2018.

doi: 10.1111/mice.12375

[12]   A. B. Khajwal, C-S. Cheng, and A. Noshadravan, "Post-disaster Damage Classification Based on Deep Multi-view Image Fusion," *Comput. Civ. Infrastruct. Eng.*, vol. 38, no. 4, pp. 528–544, 2023.

doi: 10.1111/mice.12890

[13]   J. Sublime and E. Kalinicheva, "Automatic Post-Disaster Damage Mapping Using Deep-Learning Techniques for Change Detection : Case Study of the Tohoku Tsunami," *Remote Sens.*, vol. 11, no. 1123, 2019.

doi: 10.3390/rs11091123

[14]   J.-P. Pinelli, D. Roueche, T. Kijewski-Correa, F. Plaz, D. Prevatt, I. Zisis, A. Elawady, F. Haan, S. Pei, K. Gurley, A. Rasouli, M. Refan, L. Rhode-Barbarigos, M. Moravej,

"Overview of Damage Observed in Regional Construction During the Passage of Hurricane Irma Over the State of Florida," 2018.

[15] B. J. Adams, "Improved Disaster Management Through Post-earthquake Building Damage Assessment Using Multitemporal Satellite Imagery," in *Proceedings of the ISPRS XXth Congress*, 2004, vol. 35, pp. 12–23.

[16] S. Hashitera, M. Kohiyama, N. Maki, and H. Fujita, "Use of DMSP-OLS Images for Early Identification of Impacted Areas due to the 1999 Marmara Earthquake Disaster," in *Proceedings of the 20th Asian Conference on Remote Sensing*, vol. 2, pp. 1291–1296, 1999.

[17] M. Estrada, M. Kohiyama, M. Matsuoka, and F. Yamazaki, "Detection of Damage due to the 2001 El Salvador Earthquake Using Landsat Images," in *Proceedings of the 22nd Asian Conference on Remote Sensing*, vol. 2, pp. 1372–1377, 2001.

[18] F. Yamazaki and M. Matsuoka, "Remote Sensing Technologies in Post-disaster Damage Assessment," *J. Earthq. Tsunami*, vol. 1, no. 03, pp. 193–210, 2007.

[19] C-S. Cheng, A. H. Behzadan, and A. Noshadravan, "Deep Learning for Post-hurricane Aerial Damage Assessment of Buildings," *Comput. Civ. Infrastruct. Eng.*, vol. 36, no. 6, pp. 695–710, 2021.

doi: 10.1111/mice.12658

[20] P. Rie, "Buildings Covered With the Water," *Pexels*. https://www.pexels.com/photo/buildings-covered-with-the-water-14823611/

[21] M. A. A. Hoque, S. Phinn, and C. Roelfsema, "A Systematic Review of Tropical Cyclone Disaster Management Research Using Remote Sensing and Spatial Analysis," *Ocean Coast. Manag.*, vol. 146, no. February, pp. 109–120, 2017.

doi: 10.1016/j.ocecoaman.2017.07.001

[22] D. H. A. Al-Khudhairy, I. Caravaggi, and S. Giada, "Structural Damage Assessments from Ikonos Data Using Change Detection, Object-oriented Segmentation, and Classification Techniques," *Photogramm. Eng. Remote Sensing*, vol. 71, no. 7, pp. 825–837, 2005.
doi: 10.14358/PERS.71.7.825

[23] C. F. Barnes, H. Fritz, and J. Yoo, "Hurricane Disaster Assessments with Image-driven Data Mining in High-resolution Satellite Imagery," *IEEE Trans. Geosci. Remote Sens.*, vol. 45, no. 6, pp. 1631–1640, 2007.
doi: 10.1109/TGRS.2007.890808

[24] J. Lee, J. Z. Xu, K. Sohn, W. Lu, D. Berthelot, I. Gur, P. Khaitan, K-W. Huang, K. Koupparis, B. Kowatsch, "Assessing Post-Disaster Damage from Satellite Imagery using Semi-Supervised Learning Techniques," pp. 1–10, 2020.

[25] V. Oludare, L. Kezebou, K. Panetta, and S. Agaian, "Semi-supervised Learning for Improved Post-disaster Damage Assessment from Satellite Imagery," *Proceedings Volume 11734, Multimodal Image Exploitation and Learning 2021*.
doi.org/10.1117/12.2586232 2021. doi: doi.org/10.1117/12.2586232.

[26] J. Shao, L. Tang, M. Liu, G. Shao, L. Sun, and Q. Qiu, "BDD-Net : A General Protocol for Mapping Buildings Damaged by a Wide Range of Disasters Based on Satellite Imagery," *Remote Sens.*, vol. 12, no. 1670, 2020.
doi.org/10.3390/rs12101670

[27] Y. Shen, S. Zhu, T. Yang, C. Chen, D. Pan, J. Chen, L. Xiao, Q. Du, "BDANet : Multiscale Convolutional Neural Network With Cross-Directional Attention for Building Damage Assessment From Satellite Images," *IEEE Trans. Geosci. Remote Sens.*, vol. 60, pp. 1–14, 2022.

doi: 10.1109/TGRS.2021.3080580

[28]   Q. D. Cao and Y. Choe, "Building Damage Annotation on Post-hurricane Satellite Imagery Based on Convolutional Neural Networks," *Nat. Hazards*, vol. 103, no. 3, pp. 3357–3376, 2020.

doi: 10.1007/s11069-020-04133-2

[29]   S. Ghaffarian and N. Kerle, "Towards Post-disaster Debris Identification For Precise Damage and Recovery Assessments from UAV and Satellite Images," *Int. Arch. Photogramm. Remote Sens. Spat. Inf. Sci.*, vol. XLII, no. ISPRS Geospatial Week 2019, pp. 10–14, 2019.

doi.org/10.5194/isprs-archives-XLII-2-W13-297-2019

[30]   S. Dotel, A. Shrestha, A. Bhusal, R. Pathak, A. Shakya, and S. P. Panday, "Disaster Assessment from Satellite Imagery by Analysing Topographical Features Using Deep Learning," in *IVSP '20: Proceedings of the 2020 2nd International Conference on Image, Video and Signal Processing*, 2020, pp. 86–92.

doi: 10.1145/3388818.3389160

[31]   P. Berezina and D. Liu, "Hurricane Damage Assessment Using Coupled Convolutional Neural Networks: a Case Study of Hurricane Michael," *Geomatics, Nat. Hazards Risk*, vol. 13, no. 1, pp. 414–431, Dec. 2022.

doi: 10.1080/19475705.2022.2030414

[32]   J. Zapata, "Aerial Photography of Building," *Pexels*. https://www.pexels.com/photo/aerial-photography-of-building-1434273/

[33]   R. Zhang, K. Duan, S. You, F. Wang, and S. Tan, "A Novel Remote Sensing Detection Method for Buildings Damaged by Earthquake Based on Multiscale Adaptive Multiple

Feature Fusion," *Geomatics, Nat. Hazards Risk*, vol. 11, no. 1, pp. 1912–1938, 2020. doi: 10.1080/19475705.2020.1818637

[34] S. Tilon, F. Nex, N. Kerle, and G. Vosselman, "Post-disaster Building Damage Detection from Earth Observation Imagery Using Unsupervised and Transferable Anomaly Detecting Generative Adversarial Networks," *Remote Sens.*, vol. 12, no. 24: 4193, 2020. doi: 10.3390/rs12244193

[35] M. Kirscht and C. Rinke, "3D Reconstruction of Buildings and Vegetation from Synthetic Aperture Radar (SAR) Images," 1998.

[36] U. N. Umbra News, "Umbra Releases Aerial Test Data," *Umbra*, 2021. https://umbra.space/blog/umbra-releases-aerial-test-data/

[37] X. Shen, D. Wang, K. Mao, E. Anagnostou, and Y. Hong, "Inundation Extent Mapping by Synthetic Aperture Radar : A Review," *Remote Sens.*, vol. 11, no. 7: 879, 2019. doi: 10.3390/rs11070879

[38] V. Scotti, M. Giannini, and F. Cioffi, "Enhanced Flood Mapping Using Synthetic Aperture Radar (SAR) Images , Hydraulic Modelling , and Social Media : A Case Study of Hurricane Harvey (Houston , TX)," *Flood Risk Manag.*, vol. 13, no. 4, pp. 1–18, 2020. doi: 10.1111/jfr3.12647

[39] J. W. Kosianka, M. A. Allen, and N. Rodgers, "Pre- and Post-storm Hurricane Monitoring via Data-driven SAR-based Analytics," in *Proc. SPIE 11888, Space, Satellites, and Sustainability II*, vol. 11888F, Oct. 2021. doi: 10.1117/12.2600975

[40] M. Chini, R. Pelich, L. Pulvirenti, N. Pierdicca, R. Hostache, and P. Matgen, "Sentinel-1 InSAR Coherence to Detect Floodwater in Urban Areas : Houston and Hurricane Harvey as

A Test Case," *Remote Sens.*, vol. 11, no. 2: 107, 2019.

doi: 10.3390/rs11020107

[41] K. Dai, Q. Xu, Z. Li, R. Tomas, X. Fan, X. Dong, W. Li, Z. Zhou, J. Gou, P. Ran, "Post-disaster assessment of 2017 catastrophic Xinmo landslide (China) by spaceborne SAR interferometry," *Landslides*, no. 16, pp. 1189–1199, 2019.

doi: 10.1007/s10346-019-01152-4

[42] S. Saha, F. Bovolo, and L. Bruzzone, "Destroyed-buildings Detection from VHR SAR Images Using Deep Features," in *Proc. SPIE Image and Signal Processing for Remote Sensing XXIV*, Oct. 2018, vol. 10789, p. 107890Z.

doi: 10.1117/12.2325149

[43] E. Ferrentino, F. Nunziata, C. Bignami, L. Graziani, L. Maramai, M. Migliaccio, "Multi-polarization C-band SAR Imagery to Quantify Damage Levels due to the Central Italy Earthquake" *Int. J. Remote Sens.*, vol. 42, no. 15, pp. 5969–5984, 2021.

doi: 10.1080/01431161.2021.1933247

[44] X. Zhuge, "Short-Range Ultra-Wideband Imaging with Multiple-Input Multiple-Output Arrays," TU Delft, 2010.

[45] E. Alvarado, "237 Ways Drone Applications Revolutionize Business," *237 Ways Drone Applications Revolutionize Business*, 2021. https://droneii.com/237-ways-drone-applications-revolutionize-business

[46] H. S. Munawar, A. W. A. Hammad, S. T. Waller, M. J. Thaheem, and A. Shrestha, "An Integrated Approach for Post-disaster Flood Management via the Use of Cutting-edge Technologies and UAVs: A Review," *Sustain.*, vol. 13, no. 14, 2021.

doi: 10.3390/su13147925

[47] C. A. F. Ezequiel *et al.*, "UAV Aerial Imaging Applications for Post-disaster Assessment, Environmental Management and Infrastructure Development," *2014 Int. Conf. Unmanned Aircr. Syst. ICUAS 2014 - Conf. Proc.*, pp. 274–283, 2014.

doi: 10.1109/ICUAS.2014.6842266

[48] A. Calantropio, F. Chiabrando, M. Codastefano, and E. Bourke, "Deep Learning for Automatic Building Damage Assessment : Application in Post-disaster Scenarios Using UAV Data," in *ISPRS Annals of the Photogrammetry, Remote Sensing and Spatial Information Sciences*, 2021, vol. V–1, pp. 113–120.

[49] R. Yu, P. Li, J. Shan, and H. Zhu, "Structural State Estimation of Earthquake-damaged Building Structures by Using UAV Photogrammetry and Point Cloud Segmentation," *Measurement*, vol. 202, p. 111858, 2022.

doi: https://doi.org/10.1016/j.measurement.2022.111858

[50] M. Schaefer, R. Teeuw, S. Day, and D. Zekkos, "Low-cost UAV Surveys of Hurricane Damage in Dominica: Automated Processing with Co-registration of Pre-hurricane Imagery for Change Analysis," *Nat. Hazards*, vol. 101, no. 3, pp. 755–784, 2020.

doi: 10.1007/s11069-020-03893-1

[51] J. Yeom, Y. Han, A. Chang, and J. Jung, "Hurricane Building Damage Assessment using Post-Disaster UAV Data," in *IGARSS 2019 - 2019 IEEE International Geoscience and Remote Sensing Symposium*, pp. 9867–9870, 2019.

doi: 10.1109/IGARSS.2019.8900477

[52] Z. Zhou, J. Gong, and X. Hu, "Community-scale Multi-level Post-hurricane Damage Assessment of Residential Buildings using Multi-temporal Airborne LiDAR Data," *Autom. Constr.*, vol. 98, pp. 30–45, 2019.

doi: 10.1016/j.autcon.2018.10.018

[53]   K.-S. Wu, Y. He, Q. Chen, and Y. Zheng, "Analysis on the Damage and Recovery of Typhoon Disaster Based on UAV Orthograph," *Microelectron. Reliab.*, vol. 107, p. 113337, 2020.

doi: https://doi.org/10.1016/j.microrel.2019.06.029

[54]   D. Whitehurst, K. Joshi, K. Kochersberger, and J. Weeks, "Post-Flood Analysis for Damage and Restoration Assessment Using Drone Imagery," *Remote Sens.*, vol. 14, no. 19: 4952, 2022.

doi: 10.3390/rs14194952

[55]   S. I. Jiménez-Jiménez, W. Ojeda-Bustamante, R. E. Ontiveros-Capurata, and M. de J. Marcial-Pablo, "Rapid Urban Flood Damage Assessment Using High Resolution Remote Sensing Data and an Object-based Approach," *Geomatics, Nat. Hazards Risk*, vol. 11, no. 1, pp. 906–927, Jan. 2020.

doi: 10.1080/19475705.2020.1760360

[56]   L. Calton and Z. Wei, "Using Artificial Neural Network Models to Assess Hurricane Damage through Transfer Learning," *Appl. Sci.*, vol. 12, no. 3: 1466, 2022.

doi: 10.3390/app12031466

[57]   J. Fu, A. Núñez, and B. De Schutter, "Real-Time UAV Routing Strategy for Monitoring and Inspection for Postdisaster Restoration of Distribution Networks," *IEEE Trans. Ind. Informatics*, vol. 18, no. 4, pp. 2582–2592, 2021.

doi: 10.1109/TII.2021.3098506

[58]   R. Nagasawa, E. Mas, L. Moya, and S. Koshimura, "Model-based Analysis of Multi-UAV Path Planning for Surveying Postdisaster Building Damage," *Sci. Rep.*, vol. 11, no. 1, p.

18588, 2021.

doi: 10.1038/s41598-021-97804-4

[59]   Y. Rubner, C. Tomasi, and L. J. Guibas, "The Earth Mover's Distance as a Metric for Image Retrieval," *Int. J. Comput. Vis.*, vol. 40, no. 2, pp. 99–121, 2000.

doi: 10.1023/A:1026543900054

[60]   Y. Pi, N. D. Nath, and A. H. Behzadan, "Detection and Semantic Segmentation of Disaster Damage in UAV Footage," *J. Comput. Civ. Eng.*, vol. 35, no. 2, p. 4020063, Mar. 2021.

doi: 10.1061/(ASCE)CP.1943-5487.0000947

[61]   N. Dalal and B. Triggs, "Histograms of Oriented Gradients for Human Detection," in *2005 IEEE Computer Society Conference on Computer Vision and Pattern Recognition (CVPR'05)*, vol. 1, pp. 886–893 vol. 1, 2005.

doi: 10.1109/CVPR.2005.177

[62]   A. R. Joshi, I. Tarte, S. Suresh, and S. G. Koolagudi, "Damage Identification and Assessment Using Image Processing on Post-disaster Satellite Imagery," in *2017 IEEE Global Humanitarian Technology Conference (GHTC)*, pp. 1–7, 2017.

doi: 10.1109/GHTC.2017.8239286

[63]   M. Azimi, A. D. Eslamlou, and G. Pekcan, "Data-Driven Structural Health Monitoring and Damage Detection through Deep Learning: State-of-the-Art Review," *Sensors*, vol. 20, no. 10: 2778, 2020.

doi: 10.3390/s20102778

[64]   S. Ghaffarian, N. Kerle, E. Pasolli, and J. Jokar Arsanjani, "Post-Disaster Building Database Updating Using Automated Deep Learning: An Integration of Pre-Disaster OpenStreetMap and Multi-Temporal Satellite Data," *Remote Sens.*, vol. 11, no. 20: 2427, 2019.

doi: 10.3390/rs11202427

[65] J. Wang *et al.*, "Knowledge-Based Detection and Assessment of Damaged Roads Using Post-Disaster High-Resolution Remote Sensing Image," *Remote Sens.*, vol. 7, no. 4. pp. 4948–4967, 2015.

doi: 10.3390/rs70404948

[66] R. M. Haralick and K. Shanmugam, "Textural Features for Image Classification," 1973.

[67] A. Abdollahi and B. Pradhan, "Urban vegetation mapping from aerial imagery using explainable AI (XAI)," *Sensors*, vol. 21, no. 14: 4738, 2021.

doi: 10.3390/s21144738

[68] E. Romano, M. Brambilla, C. Bisaglia, and A. Assirelli, "Using Image Texture Analysis to Evaluate Soil–Compost Mechanical Mixing in Organic Farms," *Agriculture*, vol. 13, no. 6, p. 1113, 2023.

doi: 10.3390/agriculture13061113

[69] Robet, C. Juliandy, Andi, Hendri, J. Hendrik, and F. A. Tarigan, "Image Road Surface Classification Based on GLCM Feature Using LGBM Classifier," *IOP Conf. Ser. Earth Environ. Sci.*, vol. 1083, no. 1, p. 12006, 2022.

doi: 10.1088/1755-1315/1083/1/012006

[70] M. H. Daneshvari, E. Nourmohammadi, M. Ameri, and B. Mojaradi, "Efficient LBP-GLCM Texture Analysis for Asphalt Pavement Raveling Detection Using eXtreme Gradient Boost," *Constr. Build. Mater.*, vol. 401, p. 132731, 2023.

doi: https://doi.org/10.1016/j.conbuildmat.2023.132731

[71] M. Kuffer, K. Pfeffer, R. Sliuzas, and I. Baud, "Extraction of Slum Areas From VHR Imagery Using GLCM Variance," *IEEE J. Sel. Top. Appl. Earth Obs. Remote Sens.*, vol. 9,

no. 5, pp. 1830–1840, 2016.

doi: 10.1109/JSTARS.2016.2538563

[72] M. O'Byrne, F. Schoefs, B. Ghosh, and V. Pakrashi, "Texture Analysis Based Damage Detection of Ageing Infrastructural Elements," *Comput. Civ. Infrastruct. Eng.*, vol. 28, no. 3, pp. 162–177, Mar. 2013.

doi: 10.1111/j.1467-8667.2012.00790.x

[73] K. Lacy, "Dramatic View of Village Houses Damaged by Thunderstorm," *Pexels*, 2020.

[74] J. Canny, "A Computational Approach to Edge Detection," no. 6, 1986.

[75] M. Gul, F. N. Catbas, and H. Hattori, "Image-Based Monitoring of Open Gears of Movable Bridges for Condition Assessment and Maintenance Decision Making," *Comput. Civ. Eng.*, vol. 29, no. 2, pp. 1–11, 2013.

doi: 10.1061/(ASCE)CP.1943-5487.0000307

[76] A.Z.H Hui, Z. Embong, A.I. Abd Hamid, R. Zainon, S.L. Wang, T.F. Ng, R.A. Hamzah, S.S. Teoh, H. Ibrahim, "Interactive Blood Vessel Segmentation from Retinal Fundus Image Based on Canny Edge Detector," *Sensors* 21, no. 19: 6380, 2021.

doi.org/10.3390/s21196380

[77] Y.-L. Chung and C.-K. Lin, "Application of a Model that Combines the YOLOv3 Object Detection Algorithm and Canny Edge Detection Algorithm to Detect Highway Accidents," *Symmetry*, vol. 12, no. 11. 2020.

doi: 10.3390/sym12111875

[78] C. Zhan, X. Duan, S. Xu, Z. Song, and M. Luo, "An Improved Moving Object Detection Algorithm Based on Frame Difference and Edge Detection," in *Fourth International Conference on Image and Graphics (ICIG 2007)*, pp. 519–523, 2007.

doi: 10.1109/ICIG.2007.153

[79] I. Abdel-Qader, O. Abudayyeh, and M. E. Kelly, "Analysis of Edge-Detection Techniques for Crack Identification in Bridges," *J. Comput. Civ. Eng.*, vol. 17, no. 4, pp. 255–263, 2003. doi: 10.1061/(asce)0887-3801(2003)17:4(255)

[80] H. Han, H. Deng, Q. Dong, X. Gu, T. Zhang, and Y. Wang, "An Advanced Otsu Method Integrated with Edge Detection and Decision Tree for Crack Detection in Highway Transportation Infrastructure," *Adv. Mater. Sci. Eng.*, vol. 2021, p. 9205509, 2021. doi: 10.1155/2021/9205509

[81] G. Wang, P. W. Tse, and M. Yuan, "Automatic Internal Crack Detection from a Sequence of Infrared Images with a Triple-threshold Canny Edge Detector," *Meas. Sci. Technol.*, vol. 29, no. 2, p. 25403, 2018. doi: 10.1088/1361-6501/aa9857

[82] E. A. Sekehravani, E. Babulak, and M. Masoodi, "Implementing Canny Edge Detection Algorithm for Noisy Image," *Bull. Electr. Eng. Informatics*, vol. 9, no. 4, pp. 1404–1410, 2020. doi: 10.11591/eei.v9i4.1837

[83] C. E. Shannon, "A Mathematical Theory of Communication," *Bell Syst. Tech. J.*, vol. 27, no. 3, pp. 379–423, 1948. doi: 10.1016/s0016-0032(23)90506-5

[84] A. Moreno-Gomez, J. P. Amezquita-Sanchez, M. Valtierra-Rodriguez, C. A. Perez-Ramirez, A. Dominguez-Gonzalez, and O. Chavez-Alegria, "EMD-Shannon Entropy-Based Methodology to Detect Incipient Damages in a Truss Structure," *Applied Sciences*, vol. 8, no. 11. 2018.

doi: 10.3390/app8112068

[85] J. P. Amezquita-Sanchez, "Entropy Algorithms for Detecting Incipient Damage in High-rise Buildings Subjected to Dynamic Vibrations," *J. Vib. Control*, vol. 27, no. 3–4, pp. 426–436, May 2020.

doi: 10.1177/1077546320929145

[86] P. V. C. Hough, "Method and Means for Recognition Complex Patterns; US Patent: US3069654A," *US Pat.*, p. 6, 1962.

[87] M. Stokkeland, K. Klausen, and T. A. Johansen, "Autonomous Visual Navigation of Unmanned Aerial Vehicle for Wind Turbine Inspection," in *2015 International Conference on Unmanned Aircraft Systems (ICUAS)*, pp. 998–1007, 2015.

doi: 10.1109/ICUAS.2015.7152389

[88] H. Long, S. Xu, and W. Gu, "An Abnormal Wind Turbine Data Cleaning Algorithm Based on Color Space Conversion and Image Feature Detection," *Appl. Energy*, vol. 311, p. 118594, 2022.

doi: https://doi.org/10.1016/j.apenergy.2022.118594

[89] F. Tschopp *et al.*, "Hough^{2}Map – Iterative Event-Based Hough Transform for High-Speed Railway Mapping," *IEEE Robot. Autom. Lett.*, vol. 6, no. 2, pp. 2745–2752, 2021.

doi: 10.1109/LRA.2021.3061404

[90] Z. Li, Y. Liu, R. Walker, R. Hayward, and J. Zhang, "Towards Automatic Power Line Detection for a UAV Surveillance System Using Pulse Coupled Neural Filter and an Improved Hough Transform," *Mach. Vis. Appl.*, vol. 21, no. 5, pp. 677–686, 2010.

doi: 10.1007/s00138-009-0206-y

[91] K. Tang, D. J. Parsons, and S. Jude, "Comparison of Automatic and Guided Learning for

Bayesian Networks to Analyse Pipe Failures in the Water Distribution System," *Reliab. Eng. Syst. Saf.*, vol. 186, pp. 24–36, 2019.

doi: 10.1016/j.ress.2019.02.001

[92] R. A. Francis, S. D. Guikema, and L. Henneman, "Bayesian Belief Networks for Predicting Drinking Water Distribution System Pipe Breaks," *Reliab. Eng. Syst. Saf.*, vol. 130, pp. 1–11, 2014.

[93] Google Maps, "Google Maps." https://www.google.com/maps/@53.5404896,-113.5000818

[94] M. Stone, "Cross-Validatory Choice and Assessment of Statistical Predictions Author (s): M . Stone Source : Journal of the Royal Statistical Society . Series B (Methodological), Vol . 36 , No . 2 Published by : Blackwell Publishing for the Royal Statistical Soci," *J. R. Stat. Soc.*, vol. 36, no. 2, pp. 111–147, 1974.